

Note: This work has not yet been peer-reviewed and is provided by the contributing author(s) via EarthArXiv.org as a means to ensure timely dissemination of scholarly and technical work on a noncommercial basis. Copyright and all rights therein are maintained by the author(s) or by other copyright owners. It is understood that all persons copying this information will adhere to the terms and constraints invoked by each author's copyright. This work may not be reposted without explicit permission of the copyright owner.

This work is under review at the *Journal of Physical Oceanography*. Copyright in this work may be transferred without further notice.

2 **Dynamics of eddying abyssal mixing layers over rough topography**

3 Henri F. Drake*

4 *Princeton University / Geophysical Fluid Dynamics Laboratory, Princeton, New Jersey,*
5 *United States*

6 *Previously, MIT–WHOI Joint Program in Oceanography/Applied Ocean Science &*
7 *Engineering, Cambridge and Woods Hole, Massachusetts, United States.*

8 Xiaozhou Ruan

9 *Massachusetts Institute of Technology, Cambridge, Massachusetts, United States*

10 Jörn Callies

11 *California Institute of Technology, Pasadena, California, United States*

12 Kelly Ogden

13 *Western University, London, Ontario, Canada*

14 Andreas M. Thurnherr

15 *Lamont-Doherty Earth Observatory, Palisades, New York, United States*

16 Raffaele Ferrari

17 *Massachusetts Institute of Technology, Cambridge, Massachusetts, United States*

18 * *Corresponding author:* Henri F. Drake, henrifdrake@gmail.com

ABSTRACT

19 The abyssal overturning circulation is thought to be primarily driven by small-scale tur-
20 bulent mixing. Diagnosed watermass transformations are dominated by rough topography
21 “hotspots”, where the bottom-enhancement of mixing causes the diffusive buoyancy flux
22 to diverge, driving widespread downwelling in the interior—only to be overwhelmed by an
23 even stronger upwelling in a thin Bottom Boundary Layer (BBL). These watermass trans-
24 formations are significantly underestimated by one-dimensional sloping boundary layer so-
25 lutions, suggesting the importance of three-dimensional physics. Here, we use a hierarchy
26 of models to generalize this one-dimensional boundary layer approach to three-dimensional
27 eddying flows over realistically rough topography. When applied to the Mid-Atlantic Ridge
28 in the Brazil Basin, the idealized simulation results are roughly consistent with available
29 observations. Integral buoyancy budgets isolate the physical processes that contribute to
30 realistically strong BBL upwelling. The downwards diffusion of buoyancy is primarily bal-
31 anced by upwelling along the canyon flanks and the surrounding abyssal hills. These flows
32 are strengthened by the restratifying effects of submesoscale baroclinic eddies on the canyon
33 flanks and by the blocking of along-ridge thermal wind within the canyon. Major topo-
34 graphic sills block along-thalweg flows from restratifying the canyon trough, resulting in the
35 continual erosion of the trough’s stratification. We propose simple modifications to the one-
36 dimensional boundary layer model which approximate each of these three-dimensional ef-
37 fects. These results provide *local* dynamical insights into mixing-driven abyssal overturning,
38 but a complete theory will also require the *non-local* coupling to the basin-scale circulation.

39 1. Introduction

40 Below the oceanic pycnocline, the vast volumes of the deep ocean are ventilated by two
41 interconnected cells of a global meridional overturning circulation (Gordon 1986). The
42 lower cell of this circulation is sourced along the coast of Antarctica, where atmospheric
43 cooling and brine rejection transform surface waters into the dense Antarctic Bottom Waters
44 (AABW) that fill the global abyssal ocean at a rate of approximately 30 Sv ($1 \text{ Sv} \equiv 10^6 \text{ m}^3/\text{s}$)
45 (Talley 2013). Since the buoyancy surface bounding AABW from above does not outcrop
46 elsewhere in the ocean, conservation of mass implies that in steady state an equal amount
47 of AABW must upwell across buoyancy surfaces (diabatically) from the abyss. Waters
48 below about 2000 m depth (corresponding to the crests of major topographic features, such
49 as mid-ocean ridges) can upwell diabatically only in the presence of interior watermass
50 transformations (e.g. small-scale turbulent mixing) or fluxes across the seafloor boundary
51 (geothermal heating) (Munk 1966; Walin 1982; Tziperman 1986; Ferrari 2014).

52 These basic inferences of a global diabatic upwelling from the abyss (e.g. Sverdrup et al.
53 1942) are also consistent with more detailed inverse modelling at regional scales (e.g. Talley
54 et al. 2003). Most notably, Hogg et al. (1982) consider the fate of 4 Sv of AABW (colder
55 than 0°C) that enters the Brazil Basin from the Southern Ocean through the Vema Channel;
56 since there are no other exits from the basin and since geothermal fluxes are relatively weak,
57 they infer that turbulent mixing must diffuse heat downward at a rate of $\mathcal{O}(3 \text{ cm}^2/\text{s})$ to
58 balance the upwelling of these waters across the 0°C isotherm.

59 Early in-situ turbulence measurements in the upper ~ 1000 m of the interior ocean sug-
60 gested turbulent diffusivities more than an order of magnitude smaller than those predicted
61 by the large-scale abyssal tracer budgets described above (Gregg 1987; Ledwell et al. 1993).

62 A subsequent celebrated field campaign in the abyssal waters of the Brazil Basin reported
63 similarly weak background diffusivities over the smooth topography of the abyssal plains,
64 but revealed diffusivities that increased downwards by several orders of magnitude over the
65 rough topography of the Mid-Atlantic Ridge (Polzin et al. 1997; Ledwell et al. 2000). Using
66 regional inverse and forward approaches, respectively, St. Laurent et al. (2001) and Huang
67 and Jin (2002) modelled the impacts of the observed bottom-enhanced mixing on the re-
68 gional circulation: bottom-enhanced mixing drove interior downwelling while upwelling was
69 restricted to a thin layer of buoyancy convergence near the bottom boundary (as opposed
70 to Munk 1966’s uniform upwelling model) and the basin-scale horizontal circulation was
71 dominated by narrow mixing-driven flows along ridge flanks (as opposed to the interior
72 geostrophic flow predicted by Stommel 1958).

73 The development of mixing parameterizations (e.g. St. Laurent and Garrett 2002; Kunze
74 et al. 2006; Polzin 2009; Melet et al. 2014; de Lavergne et al. 2020) allowed these Brazil
75 Basin results to be generalized to global abyssal watermass transformations (e.g. Nikurashin
76 and Ferrari 2013; de Lavergne et al. 2016; Kunze 2017; Cimoli et al. 2019). Based on such
77 estimates, Ferrari et al. (2016) and McDougall and Ferrari (2017) revised the conceptual
78 model of the global mixing-driven abyssal upwelling: mixing-driven diabatic upwelling is
79 confined to a thin Bottom Boundary Layer (BBL) just above the insulated (or geothermally
80 heated) seafloor, while bottom-enhanced mixing drives diabatic downwelling in the Stratified
81 Mixing Layer (SML) above; the net diabatic overturning is the small remainder of these
82 two large opposing mixing layer flows. In this emerging framework, the global overturning
83 circulation is modulated by the dynamics of thin BBLs (Callies and Ferrari 2018; Drake et al.
84 2020). Since these abyssal boundary layer flows are challenging to observe (Naveira Garabato
85 et al. 2019; Spingys et al. 2021) and are too thin to be resolved by conventional general

86 circulation models, however, they remain poorly understood (Drake 2021 and Polzin and
87 McDougall 2022 discuss outstanding questions).

88 The interpretation of the role of boundary mixing in the abyssal overturning circulation
89 (dating back to Munk 1966) has a contentious history: on the one hand, in-situ observa-
90 tions of weakly-stratified bottom mixed layers seemed to imply the existence of vigorous
91 boundary mixing (Armi 1978); on the other hand, it was argued that mixing of already
92 well-mixed waters was inefficient and thus did not lead to significant watermass transforma-
93 tion (see Garrett’s 1979 comment and Armi’s 1979b reply). Garrett (1990) later formalized
94 his criticism using sloping boundary layer theory (Phillips 1970; Wunsch 1970) and sug-
95 gested that one-dimensional flows up the sloping bottom boundary—driven by the mixing
96 itself—could provide sufficient restratification to resolve this conundrum. Based on obser-
97 vations of homogeneous layers detached from the bottom boundary (but carrying distinct
98 levels of suspended sediments), Armi (1978, 1979a) instead proposed a three-dimensional
99 boundary–interior exchange process whereby layers are rapidly mixed when they impinge
100 upon topographic features (e.g. seamounts or abyssal hills) and are eventually restratified
101 by along-isopycnal exchanges with the stratified interior.

102 In light of recent diagnostic evidence for boundary-control on the abyssal circulation (Fer-
103 rari et al. 2016), Callies (2018) revisited these ideas to test whether sloping BBL theory is
104 quantitatively consistent with observations. In his analysis of the sloping flank of the Mid-
105 Atlantic Ridge in the Brazil Basin (where co-located measurements of both abyssal mixing
106 rates and stratification are available), he found that the steady state 1D boundary layer so-
107 lution forced by the observed mixing exhibits a stratification an order of magnitude weaker
108 than observed. The watermass transformations sustained by 1D dynamics alone (Garrett

109 1990) are thus too inefficient to contribute significantly to the global abyssal overturning
110 circulation.

111 To reconcile boundary layer dynamics with observations, Callies (2018) argued the strat-
112 ification of abyssal mixing layers may be maintained by submesoscale baroclinic eddies,
113 which act to slump sloping buoyancy surfaces back to the horizontal. Mixing-driven 1D
114 boundary layer solutions are linearly unstable to submesoscale baroclinic modes (Wenegrat
115 et al. 2018; Callies 2018), in a manner similar to the well-studied analagous problem in
116 the surface mixed layer (Boccaletti et al. 2007; Fox-Kemper et al. 2008). Callies (2018)
117 simulated the finite amplitude evolution of these instabilities in a 3D generalization of the
118 1D boundary layer framework and showed that the solutions converge on a substantially
119 stronger quasi-equilibrium stratification that is more consistent with observations.

120 As acknowledged by Callies (2018), however, it is not clear to what extent such idealized so-
121 lutions are directly applicable to the mid-ocean ridge, which is characterized by particularly
122 rough topography. For example, many of the observations of bottom-enhanced mixing, strat-
123 ification, and diabatic upwelling from the region are confined to $\mathcal{O}(500\text{ m})$ -deep fracture zone
124 canyons which cut across the ridge (Polzin et al. 1997; Ledwell et al. 2000; St. Laurent et al.
125 2001; Thurnherr and Speer 2003). To account for these leading-order topographic features,
126 Ruan and Callies (2020) ran simulations of mixing-driven flow over a sinusoidal mid-ocean
127 ridge incised by an idealized Gaussian fracture zone canyon. They confirm Thurnherr and
128 Speer’s (2003) speculation that the canyon sidewalls suppress cross-canyon (or along-slope)
129 flow and thus support a vigorous up-canyon (or cross-slope) mean flow. The restratifying
130 tendency of this up-canyon mean flow is much stronger than that of either the 1D up-slope
131 flow or the submesoscale eddies on the smooth ridge flanks, implying that abyssal water-
132 mass transformations are, per unit area, four times larger within the canyons than on the

133 ridge flanks. Ruan and Callies (2020) found, however, that the simulated stratification in
134 the canyon is orders of magnitude larger than observed, suggesting their simulations are
135 still missing important physics. In addition to fracture zone canyons, mid-ocean ridges are
136 also characterized by smaller-scale anisotropic abyssal hills; these features have character-
137 istic scales taller than 1D BBLs and comparable to those of the fastest growing baroclinic
138 mode (Callies 2018; Wenegrat et al. 2018), so we would expect them to affect both mean
139 and eddying circulations. Within the fracture zone canyons, abyssal hills often manifest
140 as sills that substantially block or constrain the deep up-slope flow (Thurnherr et al. 2005;
141 Dell 2013; Dell and Pratt 2015); hydraulic acceleration over the sill produces relatively large
142 velocities also associated with locally enhanced turbulence (Clément et al. 2017).

143 Here, we use a hierarchy of analytical and numerical solutions to bridge the gap between
144 idealized 1D BBLs and the complexity of observed flows in a region scarred by a fracture
145 zone canyon and dotted with abyssal hills. In Section 2, we review key insights from the
146 1D BBL buoyancy budget and derive a generalized buoyancy budget that permits topo-
147 graphic variations and spatio-temporal eddy correlations. In Section 3, we describe the
148 “slope-aligned” simulation configuration which leverages a coordinate frame aligned with
149 the mean topographic slope to allow restratification by mean up-slope flow across a uniform
150 background vertical buoyancy gradient. In Section 4, we describe the simulated mixing
151 layer flows in a simulation with realistic topography and show they are qualitatively con-
152 sistent with available observations. In Section 5, we present simulated buoyancy budgets,
153 and show a balance between bottom-enhanced mixing, submesoscale eddy fluxes, and the
154 cross-slope mean flow. By progressively simplifying the configuration in a hierarchy of mod-
155 els framework (Held 2005), we isolate the roles of individual physical processes in setting
156 the near-boundary stratification. In Section 6, we discuss how our results bridge the gap

157 between interpretations of in-situ observations (e.g. Armi 1978; Thurnherr and Speer 2003;
 158 Thurnherr et al. 2020) and 1D BBL theory (e.g. Garrett 1979; Garrett et al. 1993), and
 159 how they illustrate—at a regional scale—the control of abyssal mixing layers on an “upside-
 160 down” abyssal overturning circulation (Ferrari et al. 2016). We conclude that a combination
 161 of mixing-driven up-slope flows, submesoscale baroclinic eddies, and topographic control
 162 are required to maintain a steady state near-boundary stratification consistent with in-situ
 163 observations and a finite global abyssal overturning circulation.

164 2. Theory

165 We review the derivation and results of sloping boundary layer theory in Sections 2a,b in
 166 anticipation of our generalization to three-dimensional flows over rough sloping topography
 167 in Section 2c.

168 *a. Slope-aligned equations*

169 In sloping boundary layer theory (Wunsch 1970; Phillips 1970; Garrett et al. 1993; Thomp-
 170 son and Johnson 1996; Callies 2018; Holmes and McDougall 2020), analytical progress is
 171 achieved by modelling the system in a coordinate frame aligned with its mean topographic
 172 slope, rather than the typical coordinate frame $(\hat{x}, \hat{y}, \hat{z})$ with \hat{z} aligned with gravity. It is
 173 useful to decompose the buoyancy $B = N^2 \hat{z} + b$ into a background component $N^2 \hat{z}$, where
 174 N^2 is a constant vertical buoyancy gradient, and a perturbation component $b(\hat{x}, \hat{y}, \hat{z}, t)$; the
 175 background buoyancy is assumed to be in hydrostatic balance with a background pressure
 176 and we similarly decompose $P = \frac{1}{2} N^2 \hat{z}^2 + p$. Then, we rotate the coordinate system to a
 177 coordinate frame aligned with the mean-slope $(x, y, z) \equiv (\hat{x} \cos \theta + \hat{z} \sin \theta, \hat{y}, \hat{z} \cos \theta - \hat{x} \sin \theta)$,
 178 where θ is the region’s average slope angle in the \hat{x} -direction (e.g. dashed black lines in Fig-

179 ure 3b). For small slopes¹ $\tan \theta \ll 1$, the hydrostatic Boussinesq equations in the mean-slope
 180 coordinates are, at leading order, given by

$$u_t + \mathbf{u} \cdot \nabla u - fv \cos \theta = -p_x + b \sin \theta + \nabla \cdot (\nu \nabla u), \quad (1)$$

$$v_t + \mathbf{u} \cdot \nabla v + fu \cos \theta = -p_y + \nabla \cdot (\nu \nabla v), \quad (2)$$

$$p_z = b \cos \theta, \quad (3)$$

$$\nabla \cdot \mathbf{u} = 0, \quad (4)$$

$$b_t + \mathbf{u} \cdot \nabla b + N^2(w \cos \theta + u \sin \theta) = \nabla \cdot [\kappa (N^2 \cos \theta \mathbf{z} + \nabla b)], \quad (5)$$

181 where subscripts represent partial derivatives, ∇ is the gradient operator, u is the along-
 182 canyon (or cross-slope) velocity, v is the cross-canyon (or along-slope) velocity, w is the
 183 slope-normal velocity, f is a constant Coriolis parameter, κ is an isotropic eddy diffusivity,
 184 and $\nu = \sigma \kappa$ is an isotropic eddy viscosity determined by the turbulent Prandtl number
 185 σ . The rotated along-canyon \mathbf{x} -momentum equation is identical in form to the zonal $\hat{\mathbf{x}}$ -
 186 momentum equation with the exception of the small but dynamically significant projection
 187 of the perturbation buoyancy force $b\hat{\mathbf{z}}$ on \mathbf{x} .

188 The anomalous seafloor depth, relative to the mean slope, is given by

$$d(x, y) = \hat{d}(\hat{x}, \hat{y}) + \hat{x} \tan \theta \quad (6)$$

189 We set $z = 0$ along the sloping plane that intersects the point with the greatest anomalous
 190 seafloor depth, $\max(d)$ (see Figure 2). Boundary conditions at the seafloor, $z = \max(d) -$

¹While $\sin \theta \simeq \theta$ and $\cos \theta \simeq 1$ in this limit, we retain these geometric terms explicitly so they are not forgotten.

191 $d(x, y)$, are $\mathbf{u} = 0$ (no-slip² and no-normal-flow) and $\mathbf{n} \cdot (\kappa \nabla B) = 0$ (insulating³), where \mathbf{n}
 192 is a unit vector normal to the boundary.

193 *b. Smooth planar slopes and steady 1D dynamics*

194 Assuming a constant topographic slope ($d \equiv 0$) and mixing rates that vary only in the
 195 slope-normal direction, the equilibrium solution reduces to

$$-fv \cos \theta = b \sin \theta + \partial_z (\nu u_z), \quad (7)$$

$$fu \cos \theta = \partial_z (\nu v_z), \quad (8)$$

$$p_z = b \cos \theta, \quad (9)$$

$$uN^2 \sin \theta = \partial_z [\kappa (N^2 \cos \theta + b_z)], \quad (10)$$

196 where the continuity equation $w_z = 0$ combines with the no-normal-flow bottom boundary
 197 condition at $z = 0$ to require $w \equiv 0$ everywhere (no slope-normal exchange). These equa-
 198 tions can be solved analytically in the case of constant parameter values (Wunsch 1970;
 199 Phillips 1970; Thorpe 1987; Garrett 1990), or approximately for varying parameters in some
 200 asymptotic limits (Salmun et al. 1991; Callies 2018). In either case, the slope Burger number
 201 $S \equiv N^2 \tan^2 \theta / f^2$ and the BBL thickness

$$\delta \equiv q^{-1} = \sqrt{\frac{2\nu}{f}} (1 + S\sigma)^{-\frac{1}{4}}, \quad (11)$$

202 emerge as key parameters. We recognize δ as the Ekman layer thickness $\delta_E \equiv \sqrt{\frac{2\nu}{f}}$, modified
 203 by buoyancy effects at the sloping boundary; for typical abyssal values, $S \ll 1$ and $\sigma = \mathcal{O}(1)$
 204 such that buoyancy effects are weak (Thurnherr and Speer 2003).

²While applying a bottom drag to match the unresolved Reynolds' stresses in the turbulent log-layer would be a more defensible option (Taylor and Shaw 1920), we choose the no-slip condition for a closer correspondence to 1D BBL models.

³Geothermal heating is thought to contribute negligibly to abyssal watermass transformations in the BBTR canyon region (Thurnherr et al. 2020), so we ignore it for simplicity here.

205 Recalling the crucial assumption of a constant background vertical stratification N^2 , the
 206 slope-aligned buoyancy equation (10) describes a direct balance between slope-normal diffu-
 207 sion of heat downwards towards the boundary and cross-slope advection against the constant
 208 background buoyancy gradient; this balance is a near-boundary analog of Munk's (1966)
 209 classic interior ocean vertical balance. This is best illustrated by integrating (10) in the
 210 slope-normal direction,

$$\psi(z) \equiv \int_0^z u \, dz = \kappa \cot \theta (B_z/N^2 \cos \theta) = \kappa \cot \theta (1 + b_z/N^2 \cos \theta), \quad (12)$$

211 where ψ is the up-slope transport (per along-slope unit length) and we have invoked the
 212 insulating bottom boundary condition on the full stratification, $B_z = 0$ at $z = 0$.

213 Consider the case of exponentially bottom-enhanced mixing, $\kappa(z) = \kappa_{\text{BG}} + \kappa_{\text{BOT}} e^{-z/h}$ with
 214 $\kappa_{\text{BOT}}/\kappa_{\text{BG}} \gg 1$. Equation (12) reveals two keys insights:

- 215 1. The net up-slope transport, integrated over both the upwelling BBL and the down-
 216 welling SML, converges to the negligibly small value⁴

$$\psi_\infty \equiv \psi(z \rightarrow \infty) = \kappa_{\text{BG}} \cot \theta \quad (\text{the 1D integral constraint}) \quad (13)$$

217 since far from the boundary $b_z \rightarrow 0$ (Thorpe 1987) and both $\kappa(z) \rightarrow \kappa_{\text{BG}}$ and $\cot \theta$ are
 218 small.

- 219 2. Maximal up-slope transport in the BBL is achieved when both κ is large (i.e. near the
 220 boundary) and B_z is large (strong restratification). If the stratification is maintained
 221 near the background value $N^2 \cos \theta$ where the diffusivity is large (i.e. $z \ll h$) then
 222 the up-slope transport in the BBL reaches an upper bound $\max\{\psi\} \simeq \kappa_{\text{BOT}} \cot \theta =$
 223 $\frac{\kappa_{\text{BOT}}}{\kappa_{\text{BG}}} \psi_\infty \gg \psi_\infty$.

⁴While $\psi_\infty \rightarrow \infty$ as $\theta \rightarrow 0$, the adjustment timescales also grows, $\tau_{\text{BBL}} = \delta^2/\kappa_{\text{BG}} \propto \cot \theta \rightarrow \infty$, making it more likely that other dynamics disrupt the approach to equilibrium.

224 Callies (2018) derives approximate but analytical boundary layer solutions to the steady
 225 1D system (eqs. 7–10) for bottom-enhanced mixing. In the abyssal ocean regime with typical
 226 values of $S\sigma \ll 1$, the equilibrium stratification B_z is approximately inversely proportional
 227 to κ in the SML (their eq. 10; Figure 1a, solid lines), such that the diffusive buoyancy flux
 228 $\kappa B_z \simeq \kappa_{\text{BG}} N^2 \cos \theta$ is constant and finite buoyancy flux convergence occurs only within the
 229 thin BBL. Since the BBL stratification is reduced to roughly $B_z \approx \frac{\kappa_{\text{BG}}}{\kappa_{\text{BOT}}} N^2 \cos \theta$ (Figure 1a,
 230 solid lines) and near-boundary mixing is thus inefficient, up-slope BBL transport is roughly
 231 equal to the negligibly small integral constraint (13), $\max\{\psi\} \simeq \kappa_{\text{BG}} \cot \theta$ (Figure 8a, dotted
 232 and dashed lines). This weak BBL upwelling and negligible SML downwelling contrasts with
 233 the strong bi-directional flows inferred from watermass transformation analyses (Ferrari et al.
 234 2016; McDougall and Ferrari 2017).

235 *c. Rough topography and eddy fluxes*

236 We now derive the 3D BBL buoyancy budget, which allows for topographic and flow
 237 variations along the plane of the slope. Consider the buoyancy budget for a volume \mathcal{V}
 238 within a height z above the mean slope (Figure 2):

$$\iiint_{\mathcal{V}(z' < z)} b_t \, dV = \iint_{\mathcal{A} \equiv \partial\mathcal{V}(z' < z)} (-\mathbf{u}B + \kappa \nabla B) \cdot \mathbf{n} \, dA, \quad (14)$$

239 where we use the divergence theorem to rewrite the right-hand side terms in terms of
 240 fluxes normal to the bounding surface $\partial\mathcal{V}$ (Figure 2). Fluxes through the seafloor at
 241 $z' = \max(d) - d(x, y)$ vanish due to the no-flow and insulating bottom boundary condi-
 242 tions. Motivated by the simulations in Section 3, we assume fluxes through cross-slope and
 243 along-slope boundaries cancel due to periodicity (e.g. $b(x) = b(x + L_x)$), except for the

244 up-slope flow across the background buoyancy gradient (recall $B = N^2 \hat{z} + b$),

$$\iint_{\mathcal{A}(x+L_x; z' \leq z)} (-uB) \, dydz' - \iint_{\mathcal{A}(x; z' \leq z)} (-uB) \, dydz' = -N^2 L_x \sin \theta \iint_{\mathcal{A}(x; z' \leq z)} u \, dydz' \quad (15)$$

245 This, combined with the slope-normal component of the flux through the $z' = z$ surface,

246 gives

$$\underbrace{\iiint_{\mathcal{V}(z' \leq z)} b_t \, dV}_{\text{LHS}} = \underbrace{-\langle -\kappa B_z \rangle}_{\text{Mixing}} \underbrace{-\langle wb \rangle}_{\text{Eddies}} \underbrace{-N^2 L_x \sin \theta \Psi}_{\text{Mean Flow}}, \quad (16)$$

RHS

247 where we define $\langle \phi \rangle \equiv \iint_{\mathcal{A}(z)} \phi \, dx dy$ as the slope-integral operation and $\Psi(z) \equiv$

248 $\iint_{\mathcal{A}(x; z' \leq z)} u \, dydz'$ as the up-slope transport across the periodic boundary (Figure 2a). At

249 equilibrium, the form of the generalized volume-integral buoyancy equation (16) is simi-

250 lar to the 1D transport equation (12), although there is now an additional eddy flux of

251 buoyancy towards or away from the boundary, and the turbulent buoyancy flux may be

252 modified by along- and cross-slope correlations between κ and B_z . Assuming a steady state

253 and integrating up far into the interior, where $\kappa \rightarrow \kappa_{\text{BG}}$ and the perturbations vanish, we

254 recover the integral constraint (13) on the net up-slope transport from the 1D solution,

$$255 \Psi_\infty / L_y = \kappa_{\text{BG}} \cot \theta.$$

256 Callies (2018) proposes a simple parameterization of restratification by 3D submesoscale

257 baroclinic eddies as a way to account for these missing physics in the 1D boundary layer

258 solution. The main effect of baroclinic eddies is to extract available potential energy from

259 the mean flow by slumping sloping buoyancy surfaces back towards the horizontal, thereby

260 maintaining a realistically-large near-bottom stratification; this adiabatic process is most

261 conventionally parameterized as an eddy overturning circulation (Gent and McWilliams

262 1990; Fox-Kemper et al. 2008). Taking advantage of thermal wind balance ($fv_z = b_x$), the

263 slumping of isopycnals by baroclinic instability—which decreases horizontal buoyancy gra-
 264 dients $b_{\hat{x}}$ —can equivalently be parameterized as a reduction in the vertical shear v_z , e.g. by
 265 enhanced vertical momentum diffusion (Rhines and Young 1982; Greatbatch and Lamb 1990;
 266 Young 2011). We provide a derivation of this closure in the Appendix, in which we apply
 267 Andrews and McIntyre’s (1976) Transformed Eulerian Mean and Gent and McWilliams’s
 268 (1990)’s baroclinic eddy parameterization scheme to the slope-aligned framework.

269 Following Callies (2018), we thus parameterize submesoscale eddy restratification by arti-
 270 ficially increasing the vertical eddy viscosity $\nu = \sigma\kappa$. Unlike Callies (2018), who simply tune
 271 $\sigma = 230$ to match the mean behavior of their 3D model, however, we: 1) only enhance the
 272 viscosity $\nu_v = \sigma_v\kappa$ acting on the along-slope thermal wind (as in Holmes et al. 2019) since
 273 the available potential energy that fuels the instabilities is stored in cross-slope buoyancy
 274 gradients; 2) we allow the eddy viscosity to have vertical structure, $\sigma_v = \sigma_v(z)$, and 3) we
 275 estimate the magnitude and structure of $\sigma_v(z)$ from the eddy fluxes resolved by a 3D model
 276 (Figure 1b; see Appendix). We refer to $\Psi + \frac{\langle wb \rangle}{N^2 \sin \theta L_x}$ as the cross-slope *residual* transport
 277 (analogous to that of the Southern Ocean, e.g. Marshall and Radko 2003), since the eddy
 278 flux term is equal to the eddy overturning streamfunction in the limit of stationary and
 279 adiabatic eddies, which is applicable outside of the thin BBL (Figure 11c; see Appendix).

280 Applying this simple closure to the 1D model results in weakening of the slope-normal
 281 shear of the along-slope flow and, because of the approximate thermal wind balance $fv_z \simeq$
 282 $b_z \sin \theta$ that holds in the SML (eq. 8), results in a corresponding weakening of the negative
 283 perturbation stratification b_z (equivalent to a strengthening of the total stratification B_z ;
 284 compare dash-dotted and solid lines in Figure 1a). In this context, the 1D model’s up-slope
 285 transport ψ is re-interpreted as the residual transport, since it also includes the eddy-induced
 286 overturning. At equilibrium, this parameterized eddy restratification triples B_z and thus also

287 κB_z and the residual flow ψ at the top of the 1D solution’s BBL (Figure 1a and Figure 8a,b),
288 bringing the watermass transformations of the 1D BBL more in line with the basin-scale
289 overturning (Morris et al. 2001; Callies 2018).

290 **3. Numerical model setup**

291 We simulate 3D mixing-driven flows using the hydrostatic Boussinesq equations in the
292 MIT General Circulation Model (MITgcm; Marshall et al. 1997). For simplicity, we assume a
293 linear equation of state; because temperature units are more intuitive, we use temperature T
294 and buoyancy $b \equiv g\alpha T$ interchangeably throughout, where $g = 9.81 \text{ m/s}^2$ is the gravitational
295 acceleration and $\alpha = 2 \times 10^{-4} \text{ }^\circ\text{C}^{-1}$ is a constant thermal expansion coefficient.

296 *a. Realistic bathymetry*

297 Most of the results describe a core realistic-bathymetry simulation of the Brazil Basin sub-
298 region sampled by both the Brazil Basin Tracer Release Experiment (BBTRE, Ledwell et al.
299 2000) and Dynamics of the Mid-Ocean Ridge Experiment (DoMORE, Clément et al. 2017),
300 located on the western flank of the Mid-Atlantic Ridge. We extract the Brazil Basin’s
301 seafloor topography from the Global Bathymetry and Topography at 15 Arc Sec dataset
302 (SRTM15+; Tozer et al. 2019), which includes many more multibeam measurements than
303 previous products (e.g. Smith and Sandwell 1997) and thus better resolves both the BBTRE
304 fracture zone canyon at $21^\circ 30' \text{ S}$ and the smaller-scale abyssal hills characteristic of mid-
305 ocean ridges (Figure 3a). We interpolate the bathymetry onto a locally tangent Cartesian
306 grid $(\hat{x}, \hat{y}, \hat{z})$ aligned with the BBTRE canyon, where \hat{x} denotes the along-canyon dimension
307 and \hat{y} denotes the cross-canyon dimension (Figure 3a), and produce a gridded bathymetry
308 field $\hat{d}(\hat{x}, \hat{y})$. The simulated canyon stretches from a few km west of the Tracer Release

309 Experiment site around 18.5°W (Ledwell et al. 2000) to a few km east of the DoMORE sill
310 that dramatically constrains the up-canyon flow at 14.5°W (Clément et al. 2017).

311 *b. Implementing the perturbation Boussinesq equations in the mean-slope coordinate frame*

312 Following Section 2a, we solve equations (1–5) in a coordinate frame aligned with the
313 domain’s mean slope. Equations (1–5) are solved in terms of the perturbation variables,
314 with the background buoyancy field $N^2\hat{z}$ entering only indirectly via linear and inhomogeneous
315 terms in the perturbation buoyancy equation, implemented as additional explicit
316 tendency terms in the MITgcm. To stabilize the numerical solution without damping sub-
317 mesoscale eddies, we additionally implement horizontal (in the rotated frame) biharmonic
318 hyper-diffusion of momentum and buoyancy which acts only at scales close to the grid res-
319 olution. Horizontal hyper-diffusive tendencies vanish in the budgets presented here, so we
320 omit them in all of our analyses. We enforce an insulating boundary condition on the full
321 buoyancy at the seafloor: $\mathbf{n} \cdot (\kappa \nabla B) = 0$.

322 Relative to the mean slope, the anomalous seafloor topography $d(x, y) \equiv \hat{d}(\hat{x}, \hat{y}) - \hat{x} \tan \theta$ is
323 nearly continuous across the periodic boundaries in the along-canyon direction \mathbf{x} and in the
324 cross-canyon direction \mathbf{y} ; however, to eliminate any remaining discontinuities across these
325 boundaries, we join the two boundaries smoothly by linear interpolation in both \mathbf{x} and \mathbf{y} .

326 By 1) removing the uniformly-stratified background state from the prognostic variables,
327 2) formulating the model in the slope coordinate frame, and 3) making the boundary condi-
328 tions and forcing terms periodic in the (x, y) plane, we are free to apply periodic boundary
329 conditions to the perturbation state variables u , v , b , and p in both \mathbf{x} and \mathbf{y} .

330 *c. Forcing by observation-inspired bottom-enhanced turbulent mixing*

331 Following the classic one-dimensional boundary layer configuration (Wunsch 1970), we pa-
332 rameterize small-scale turbulent mixing as a slope-normal⁵ diffusive buoyancy flux $-\kappa \partial_z B \mathbf{z}$.
333 We use Callies’ (2018) self-similar height-above-bottom profile

$$\kappa(x, y, z) = \kappa(z; d) = \kappa_{\text{BG}} + \kappa_{\text{BOT}} \exp\left(-\frac{z+d}{h}\right), \quad (17)$$

334 with $\kappa_{\text{BOT}} = 1.8 \times 10^{-3} \text{ m}^2/\text{s}$, $\kappa_{\text{BG}} = 5.3 \times 10^{-5} \text{ m}^2/\text{s}$, and $h = 230 \text{ m}$; these parameter
335 values are chosen by performing a least-squares fit to the height-above-bottom-average of
336 126 microstructure profiles in the BBTRE region. The sparsity and noisiness of individual
337 mixing profiles, and disagreements in the literature about where mixing is strongest (Polzin
338 et al. 1997; St. Laurent et al. 2001; Polzin 2009; Clément et al. 2017; Thurnherr et al. 2020),
339 prohibit the formulation of a robust parameterization with a richer spatial structure. We
340 imagine this imposed bottom-enhanced mixing to represent a variety of turbulent ocean
341 processes (see Thorpe 2005), especially the breaking of internal waves (Whalen et al. 2020)
342 but also including unspecified boundary mixing processes (Armi 1978; Armi and D’Asaro
343 1980; Polzin et al. 2021).

344 *d. Numerics*

345 The horizontal grid spacing of $\Delta x = \Delta y = 600 \text{ m}$ is fine enough to permit the anticipated
346 submesoscale baroclinic turbulence, which for the 1D sloping BBL problem has a maxi-
347 mum linear growth rate near the local deformation radius $L \sim \frac{NH_{\text{ML}}}{f} = 6 \text{ km}$ (Stone 1966;
348 Wenegrat et al. 2018), where $H_{\text{ML}} \approx 250 \text{ m}$ is the thickness of the weakly-stratified bottom
349 layer (Callies 2018). Yet, the grid spacing is also coarse enough for a three-dimensional

⁵Vertical buoyancy gradients are generally much larger than horizontal gradients, so, assuming an isotropic diffusivity, the vertical (or, for small slopes $\theta \ll 1$, approximately slope-normal) components of the diffusive buoyancy flux dominate.

350 simulation of the entire 480 km by 60 km region to be computationally feasible. We set
 351 the hyper-diffusivities $\kappa_4 \equiv \nu_4 = 2 \times 10^4 \text{ m}^4/\text{s}$, the smallest value that maintains a stable
 352 solution, so that hyper-diffusion interferes minimally with diapycnal buoyancy fluxes and
 353 the growth of submesoscale instabilities (Callies 2018; Ruan and Callies 2020). In the ver-
 354 tical, a cell thickness of $\Delta z = 6 \text{ m}$ (with partial cells down to 1.2 m) marginally resolves
 355 the predicted $\mathcal{O}(10 \text{ m})$ -thick BBL. A high-resolution 1D spin-up experiment confirmed this
 356 vertical resolution is sufficient to accurately reproduce all features of the analytical solution
 357 (using Burns et al.’s 2016 Dedalus package; not shown). Starting at about 1000 m above
 358 the mean slope, the cell thickness Δz is increasingly stretched (up to $\Delta z = 50 \text{ m}$ at the top
 359 of the domain) to efficiently fit both the $h \log(\kappa_{\text{BOT}}/\kappa_{\text{BG}}) \approx 1300 \text{ m}$ vertical scale of abyssal
 360 mixing layers (Callies 2018) and the $\mathcal{O}(800 \text{ m})$ topography into a domain that spans a height
 361 $H = 2700 \text{ m}$ above the mean slope.

362 *e. Parameter regime*

363 Following Callies (2018), we assume a background far-field stratification $N =$
 364 $1.3 \times 10^{-3} \text{ s}^{-1}$ and a local Coriolis parameter $f = -5.3 \times 10^{-5} \text{ s}^{-1}$ characteristic of the
 365 BBTRE region. Applying a linear fit to the bathymetry $\hat{d}(\hat{x}, \hat{y})$ yields the domain’s av-
 366 erage topographic slope angle $\theta = 1.26 \times 10^{-3}$ in $\hat{\mathbf{x}}$. We assume that small-scale turbulent
 367 mixing acts similarly to mix buoyancy and momentum, i.e. we assume a turbulent Prandtl
 368 number of $\sigma \equiv \frac{\nu}{\kappa} = 1$. Because we resolve submesoscale instabilities, we do not need to
 369 parameterize their restratification by increasing σ . Mixing layers are thus characterized by
 370 weak stratification and gentle large-scale slopes, equating to a small slope Burger number,
 371 $S \equiv N^2 \tan^2 \theta / f^2 = 10^{-3} \ll 1$ and BBL thickness $\delta \approx 8 \text{ m}$ (eq. 11).

372 We spin up the simulations from a uniformly-stratified rest state ($b = 0, p = 0, \mathbf{u} = \mathbf{0}$). The
373 BBL adjusts rapidly on a timescale $\tau_{\text{BBL}} = \delta^2/\kappa_{\text{BOT}} = 10$ hours. While the full equilibration
374 of the solution occurs over a prohibitively long diffusive timescale characteristic of the abyssal
375 ocean interior, $\tau_{\text{INT}} = H^2/\kappa_{\text{BG}} \approx 5000$ years, buoyancy tendencies are small enough by
376 $t = 13$ years in the bottom 1000 m (see Section 5) that we consider the solution sufficiently
377 equilibrated for the analyses presented here.

378 *f. Hierarchy of progressively idealized simulations*

379 The simulations in our model hierarchy differ only in their seafloor topography, domain
380 length, and dimensionality. We progressively idealize the BBTRE canyon configuration
381 (Figure 3f): first, we remove the abyssal hills along the ridge flank and idealize the geometry
382 of the remaining canyon and sill features (“Canyon+Sill”; Figure 3e); second, we remove
383 the sill (“Canyon”; 3d); third, we remove the canyon entirely (“Smooth3D”; Figure 3c);
384 and finally, we eliminate variations along the plane of the slope, collapsing the solution
385 onto a single slope-normal dimension as in classical BBL theory (“1D”). For reference, we
386 also include some additional variants on the 1D model where we vary one parameter at
387 a time: non-rotating (“1D $_{f=0}$ ”), non-sloping (“1D $_{\theta=0}$ ”), and parameterized submesoscale
388 eddies (“1D $_{\sigma_v(z)}$ ”; see Appendix). Unless we specify otherwise, results refer to the realistic-
389 topography BBTRE simulation.

390 **4. Mixing-driven up-canyon flow, submesoscale turbulence, and stratification**

391 At quasi-equilibrium, the time-mean flow (averaged over days 5000 to 5500) is dominated
392 by a vigorous up-canyon jet along the canyon thalweg, banked along the steeper southern
393 flank of the canyon (as in Dell 2013; Ruan and Callies 2020). The up-canyon jet exhibits a

394 maximum along-canyon-averaged velocity of $\bar{u}^x = 0.75$ cm/s about 400 m above the seafloor
 395 (Figure 4a). This up-slope jet is non-uniform and partially compensated by a down-slope
 396 jet on the gentler northern flank, such that the maximum cross-canyon-averaged up-canyon
 397 velocity is reduced to $\bar{u}^y = \mathcal{O}(0.1$ cm/s) (Figure 4a,b). The up-slope jet accelerates as it
 398 spills over two major cross-canyon sills: the BBTRE sill at $x = 110$ km and the DoMORE sill
 399 at $x = 420$ km (Figure 4a,b); this acceleration and the spilling over of isopycnals at both sills
 400 is suggestive of hydraulic control⁶ (Pratt and Whitehead 2008). The vertically-integrated
 401 cross-slope transport $\int_{z=0}^H u dz$ is dominated by standing eddy features above the canyon
 402 (Figure 4c, recall $z = 0$ at the deepest point relative to the mean slope), but prominently
 403 features meandering up- and down-canyon jets when integration is restricted to just the
 404 canyon itself, $\int_{z=0}^{800\text{m}} u dz$ (Figure 4d). These simulated mixing-driven means flows can be
 405 compared against two in-situ mooring observations: the BBTRE mooring at $x = 110$ km,
 406 several km upstream of the BBTRE sill (Toole 2007; also analyzed by Thurnherr et al.
 407 2005), and a DoMORE mooring at $x = 420$ km, atop the DoMORE sill (Clément et al.
 408 2017). At the DoMORE sill, horizontal and vertical constrictions accelerate the simulated
 409 up-canyon flow to 5 cm/s over a layer $\delta z = 150$ m thick and $\delta x = 2.5$ km wide (Figure 5a).
 410 The resulting velocities are roughly constant in time, also suggestive of hydraulic control
 411 (Pratt and Whitehead 2008), and are about 25% those measured by the mooring (half as
 412 fast and half as thick; Figure 5b). By contrast, the simulated up-canyon flow at the BBTRE
 413 mooring is much weaker ($u \approx 0.75$ cm/s) but spread over a thicker ($\delta z \approx 600$ m) and wider
 414 ($\delta x \approx 5$ km) layer, such that the total up-canyon transports at the two sections are similar
 415 (Figure 5c). It is impossible to compare against observed *transports* because single mooring
 416 velocity profiles (e.g. Thurnherr et al. 2005) cannot be reliably extrapolated across the

⁶The DoMORE control section is evident from the canyon hydrography, but the BBTRE one is not (Thurnherr et al. 2005).

417 canyon, although such errors may be smaller at constrictions considerably narrower than
418 the local deformation radius (Thurnherr 2000), as at the DoMORE sill. The simulated flow
419 at the BBTRE mooring has roughly the same vertical structure as in the moored current
420 meter velocities, but about half their magnitude (Figure 5d). The relative weakness of the
421 simulated flows suggest that either the imposed microstructure-based mixing rates are biased
422 low (as suggested by Thurnherr et al. 2005 and Clément et al. 2017, and by the in prep.
423 tracer analysis by Ledwell and modelling by Odgen et al.) or that the simulation fails to
424 capture important physics.

425 Averaging the BBTRE simulation in height-above-bottom (hab) coordinates reveals that
426 the stratification generally remains close to its background value, except in the $\mathcal{O}(10\text{ m})$ -
427 thick BBL (Figure 6a, solid blue line). Upon first inspection, this result appears inconsistent
428 with observations in the canyon which, when averaged in hab, exhibit much weaker stratifi-
429 cation up to 600 m above the seafloor (Figure 6, dashed and dotted red lines). Most of this
430 discrepancy is resolved by sampling the simulation at the exact locations of the observational
431 profiles (Figure 6b), and comparing their sample mean to that of the observations (Figure 6a,
432 red lines). Since the BBTRE sampling strategy was to find as much tracer as possible, the
433 field campaign specifically focused on sampling the deep depressions in the BBTRE canyon,
434 which appear to exhibit unusually weak stratification compared to the canyon flanks, sills,
435 and the surrounding ridge flanks. However, several microstructure profiles from the 1996
436 cruise are available along the canyon crests—just north of the domain—and on average
437 exhibit similarly strong near-bottom stratification as in the simulation’s domain average
438 (Figure 6a, dashed blue line). This conditional averaging exercise clarifies the significant
439 disagreements in reported estimates of the BBTRE region’s average stratification (Polzin
440 et al. 1997; St. Laurent et al. 2001; Polzin 2009). But even accounting for sampling bias,

441 the simulated canyon is more stratified by about a factor of two relative to the observations
442 (see Section 6).

443 The time-mean view of the up-canyon circulation above filters out a rich field of subme-
444 soscale eddies which have radii comparable to the deformation radius and are trapped within
445 a few hundred meters of the seafloor, including within the $\mathcal{O}(10\text{ km})$ -wide canyon (Figure 7).
446 These eddies manifest themselves as spatial and temporal meanders of the mean up-canyon
447 jet, which in the following section we show contribute significantly to the simulation’s buoy-
448 ancancy budget and to maintaining its strong near-bottom stratification.

449 5. Buoyancy budgets: mixing, mean flow, and eddies

450 In this section, we use a hierarchy of models to elucidate the complicated dynamics that
451 support the up-canyon mean flows described in the previous section. Volume-integrated
452 buoyancy budgets (eq. 16) provide the major insights and are presented in Figure 8 for each
453 model in the hierarchy. We further separate the contributions from time-independent stand-
454 ing eddies and transient eddies. All of the solutions exhibit substantial residual tendencies
455 several hundred meters above the topography; however, within a few hundred meters of the
456 ridge flanks and within the canyons, tendencies are an order of magnitude smaller than other
457 terms in the budgets because the dynamics (vigorous mixing and submesoscale processes)
458 within the bottom few hundred meters are much faster than the weak diffusion in the inte-
459 rior (Figure 8, black). The 1D and $1D_{\sigma_v(z)}$ simulations are computationally inexpensive, so
460 we also provide their fully equilibrated solutions for context (Figure 8a,b; dotted).

461 In the classical 1D solution, a weak up-slope transport in the BBL (Figure 8a, blue line)
462 maintains a weak near-boundary stratification, although it is already much stronger than
463 in the flat-bottom after 5000 days of spin-up (Figure 9a). The evolution of the Smooth3D

464 solution follows the 1D solution closely until about 800 days, at which point the laminar
465 solution becomes unstable to submesoscale baroclinic modes which rapidly grow and equi-
466 librate at finite amplitude (Callies 2018; Wenegrat et al. 2018). At quasi-equilibrium, these
467 transient eddies advect denser waters from the SML back into the BBL (Figure 8b, orange),
468 effectively restratifying the BBL (Figure 9b) and thus strengthening the maximum diffu-
469 sive buoyancy flux (Figure 8b, red). It is helpful to interpret the combination of the mean
470 flow and the eddy fluxes as the residual circulation that advects tracers (Ferrari and Plumb
471 2003; see Appendix). In this framing, the slope-normal eddy flux nearly doubles the resid-
472 ual upwelling in the BBL (Figure 8b,a, green lines). The crude eddy parameterization in
473 $1D_{\sigma_v(z)}$ qualitatively captures this restratifying effect (Figure 9b, compare dash-dotted and
474 blue against solid grey) and enhances the residual BBL upwelling by a factor of 2–3 relative
475 to the 1D model, both transiently and at equilibrium (Figure 8b,c; solid and dotted green
476 lines, respectively). A more rigorous approach to parameterization is beyond the scope of
477 this paper.

478 The volume-integrated buoyancy budget is more complicated to interpret in the presence
479 of variable topography. In the Canyon solution, a substantial diffusive buoyancy flux con-
480 vergence drives a vigorous up-slope mean flow within the bottom 200 m along the narrow
481 trough of the canyon, producing a transport of 5 mSv (Figure 8d, blue) which is already
482 larger than the total BBL transport in the 1D model (Figure 8a, blue). This strong mean
483 flow maintains a stratification near the large background value within the canyon trough
484 (Figures 10b; 9c, orange line). Thurnherr and Speer (2003) hypothesizes this efficient re-
485 stratification is due to the canyon sidewalls blocking the along-slope thermal wind, such that
486 the momentum is redirected into the cross-slope flow. The Canyon simulation’s excellent
487 agreement with the $1D_{f=0}$ model, in which rotation is turned off and thus the along-slope

488 thermal wind is suppressed by construction, supports their hypothesis (Figure 9c; orange
 489 and dotted lines). Ruan and Callies (2020) hypothesize that flow across the steep canyon
 490 flanks with $S = \mathcal{O}(1)$ also contributes significantly to the strong stratification in the canyon.
 491 However, this hypothesis does not explain the strong stratification along the canyon thal-
 492 weg, where the cross-canyon slope goes to zero and local dynamics cannot sustain a finite
 493 stratification at equilibrium in the absence of an along-canyon topographic slope.

494 The turbulent buoyancy flux also converges around a Height Above the Mean Slope
 495 (HAMS) of $z = 800$ m, driving an additional residual upwelling of about 13 mSv from
 496 $z = 600$ m to 800 m dominated by the BBLs on the upper canyon flanks and on the smooth
 497 ridge flank surrounding the canyon (Figure 8d, green line). The upwelling along the smooth
 498 ridge flank of the Canyon simulation is about twice as large as that of the Smooth3D
 499 simulation, despite covering a smaller area, because along-slope buoyancy gradients above
 500 the canyon flanks provide an additional energy source for submesoscale instabilities (Fig-
 501 ure 10d), driving an isopycnal thickness flux between the canyon and surrounding flanks
 502 and thus maintaining a much larger stratification on the flanks (Figures 9b). In the Canyon
 503 simulation’s quasi-equilibrium state, much of the turbulent buoyancy flux divergence in the
 504 upper SML (far above the seafloor) is not yet equilibrated: the bottom-enhanced diffusion
 505 of buoyancy towards the boundary slowly cools the interior (Figure 8d, red and black lines;
 506 MacCready and Rhines (1991)).

507 In the Canyon+Sill simulation, the sill blocks up-slope flow within the trough of the canyon
 508 (Figure 8e, d). This is expected, since the up-canyon flows of $\mathcal{O}(1$ cm/s) only carry sufficient
 509 kinetic energy to lift a parcel across a stratification of $N \sim \mathcal{O}(10^{-4} - 10^{-3} \text{ s}^{-1})$ by a height
 510 $\delta_{\text{Fr}} = U/N \sim 20 - 200$ m (based on a topographic Froude number of $\text{Fr} \equiv N\delta_{\text{Fr}}/U \sim 2$),
 511 much smaller than the sill height of $h_{\text{sill}} = 800$ m and resulting in a blocked flow layer of

512 thickness $h_{\text{sill}} - \delta_{\text{Fr}}$ (Baines 1979; Winters and Armi 2012), both up- and down-stream of the
513 sill (recall the cross-slope periodicity). No up-slope mean flow is available to restratify the
514 trough of the canyon, so it slowly homogenizes due to mixing (Figure 10c; as in Dell 2013).
515 In contrast, within a slope-normal displacement δ_{Fr} of the sill, mean flows along the upper
516 parts of the two canyon flanks are able to maintain a layer of strong stratification⁷ (Figures
517 8e, 10e,f).

518 The structure of the stratification in the BBTRE simulation is qualitatively similar to
519 that of the Canyon+Sill simulation, although the rougher abyssal hill topography acts to
520 thicken the layer of enhanced stratification near the DoMORE sill height and supports a large
521 near-bottom stratification on the hilly ridge flanks surrounding the canyon (Figure 10g,h,
522 9b). The slope-normal structure of the BBTRE canyon’s buoyancy budgets (Figure 8f) is
523 remarkably similar to that of the Canyon+Sill simulation and can thus be explained as the
524 combination of the processes described—only slightly blurred in the slope-normal direction
525 by the additional topographic roughness.

526 6. Conclusions and Discussion

527 By generalizing the methods of classical 1D sloping Bottom Boundary Layer (BBL) theory
528 (Garrett et al. 1993), we construct a hierarchy of mixing-driven flow simulations that bridge
529 the gap between three-dimensional (Armi 1978) and one-dimensional (Garrett 1979) concep-
530 tual models of abyssal mixing layer restratification. Our choice to parameterize small-scale
531 turbulence as a bottom-enhanced turbulent diffusivity—inspired by local microstructure
532 measurements—considerably simplifies the analysis but may not adequately represent the

⁷Tidal velocities, omitted for simplicity here, would imply a larger excursion height, a thinner blocked flow layer, and the potential for restratification processes to penetrate deeper into the canyon trough (as hypothesized by Clément et al. 2017).

533 underlying small-scale physics (see Polzin and McDougall 2022). Nevertheless, in this con-
534 ventional prescribed-diffusivity framework we demonstrate that the homogenizing tendency
535 due to bottom-enhanced small-scale mixing is balanced by the restratifying effects of the
536 residual overturning circulation, which is a combination of mean and submesoscale eddy
537 flows (eq. 16). At equilibrium, the slow interior diffusion of heat into the abyss is balanced
538 by a weak net upwelling (eq. 13), the result of substantial cancellation of up- and down-slope
539 flows.

540 The simulations’ steady states are never achieved here due to the prohibitively slow dif-
541 fusive adjustment in the interior (MacCready and Rhines 1991); in more realistic contexts,
542 cross-slope pressure gradients due to coupling with the non-local circulation would sup-
543 port a much more rapid adjustment process (Peterson and Callies 2021). Despite the
544 non-equilibrated nature of our solutions, the slope-aligned framework permits simplified
545 buoyancy budgets which facilitate our dynamical interpretation and the derivation of an
546 eddy closure (see Appendix). Another advantage of the slope-aligned framework is that the
547 solutions are less ambiguous than previous approaches, which either require ad hoc sponge
548 layers at distant horizontal boundaries (Dell 2013) or can only be analyzed transiently be-
549 fore mixing completely homogenizes buoyancy (Ruan and Callies 2020). The slope-aligned
550 framework also permits a consistent exploration of ever more realistic configurations: from
551 a constant topographic slope—well described by 1D BBL models (Garrett et al. 1993)—
552 to the complex geometry of the region surrounding the BBTRE canyon. While the local
553 nature of the sloping BBL framework is conceptually convenient for all of the above rea-
554 sons, several important non-local factors have been ignored. For example, the inclusion of
555 cross-slope pressure gradients (Peterson and Callies 2021) or large-scale boundary currents
556 (MacCready and Rhines 1991; Naveira Garabato et al. 2019) would fundamentally alter the

557 transient spin-up problem. The periodic nature of the simulation may also overemphasize
558 topographic blocking effects since upstream topographic sills also re-appear downstream.

559 The results of our quasi-realistic simulation of the Brazil Basin Tracer Release Experiment
560 (BBTRE) reconciles two dominant boundary mixing paradigms: yes, bottom-enhanced mix-
561 ing drives a restratifying up-slope flow in the BBL (Garrett 1979, 1990); but, this flow is
562 much stronger than predicted by 1D theory due to net restratification by transient baro-
563 clinic eddies and topographic steering/blocking (Armi 1978, 1979a; Thurnherr and Speer
564 2003; Callies 2018; Ruan and Callies 2020). The net restratifying effect can to a large extent
565 be attributed to three distinct physical restratification/destratification processes:

- 566 1. slumping of isopycnals by finite-amplitude submesoscale baroclinic instabilities (Wene-
567 grat et al. 2018; Callies 2018),
- 568 2. the blocking of cross-canyon thermal winds within narrow fracture zone canyons (Thurn-
569 herr and Speer 2003; Dell 2013; Ruan and Callies 2020), and
- 570 3. the effect of sills in blocking up-canyon mean flows and homogenizing depressions well
571 below the sill height (Baines 1979; Winters and Armi 2012; Dell 2013).

572 We propose a simple parameterization for the restratifying effects of submesoscale baroclinic
573 eddies in terms of a vertically-varying enhancement of vertical momentum diffusion (see
574 Appendix). The blocking of along-slope flow by canyon walls can be captured in the 1D
575 model by inhibiting the development of along-slope thermal wind, such as by setting $f = 0$.

576 Applied to the BBTRE model, the slope-averaged buoyancy budget (16) confirms Thurn-
577 herr et al.'s (2020) hypothesis that spatial averaging reconciles the thin *local* BBL trans-
578 formations implied by vertical microstructure profiles and 1D models (e.g. Thompson and
579 Johnson 1996) with the thicker *bulk* BBL transformations implied by a decreasing topo-

580 graphic perimeter—or mixing area—with depth (Polzin 2009; Kunze et al. 2012; Holmes
581 et al. 2018): water below the canyon crest upwells in the net, while water above downwells
582 (Figure 16f). The spatial heterogeneity of the simulated up-canyon flow (Figures 5,6) may
583 explain why the buoyancy fluxes estimated from microstructure profiles are much too weak
584 to balance the upwelling transports inferred by uniformly-extrapolated moored velocity es-
585 timates (Thurnherr et al. 2005).

586 Our quasi-realistic simulations provide the first BBL- and submesoscale-resolving simula-
587 tions of the mixing-driven abyssal overturning in the Brazil Basin, complementing Huang
588 and Jin (2002) and Ogden and Ferrari’s (in prep) coarser-resolution basin-scale simulations.
589 Despite the idealization of our numerical set-up, we qualitatively reproduce key features of
590 the observations: broad up-slope flow and near-boundary stratification of $B_z \approx \mathcal{O}(10^{-7}\text{s}^{-2})$
591 along the canyon trough (Toole 2007; Ledwell et al. 2000), stronger near-bottom stratifi-
592 cation along the hills surrounding the canyon (Polzin 2009), hydraulically accelerated flow
593 over blocking sills (Clément et al. 2017), and the mean diapycnal downwelling and spreading
594 of a tracer released in the SML (Ledwell et al. 2000; see companion manuscript Drake et
595 al., in prep.). Despite this qualitative agreement, the simulated diapycnal transports within
596 the canyon are too weak—and the stratification too strong—by roughly a factor of 2. These
597 remaining discrepancies could be explained by the previously mentioned limitations of the
598 inherently local slope-aligned modelling framework and the self-similar parameterization of
599 small-scale mixing. The lack of full equilibration of the simulations could explain the too-
600 strong stratification—the 1D models become about half as stratified at equilibrium—but not
601 the too-weak up-canyon flow. Too-weak canyon mixing, on the other hand, could potentially
602 explain both biases: we speculate that microstructure-based estimates of the turbulent dif-
603 fusivity may be biased low due to sampling biases (Watson et al. 1988; Voet et al. 2015; Cael

604 and Mashayek 2021; Whalen 2021) or biases in the mixing parameterization (Ijichi et al.
 605 2020). Based on observations and basin-scale simulations of tracer spreading, respectively,
 606 Ledwell (in prep) and Ogden and Ferrari (in prep) similarly conclude that tracer observa-
 607 tions are more consistent with diffusivities about 2 times larger than those inferred from
 608 microstructure⁸.

609 The characteristic topographic features in the BBTRE (large-scale slope, canyon, and hills)
 610 are typical of mid-ocean ridges, such that the dynamics described here can be thought to
 611 apply to the global mid-ocean ridge system (with the steepness of slopes and hills modulated
 612 by the age of the rift valley and the Coriolis parameter by its latitude). The BBTRE simula-
 613 tion exhibits an instantaneous diapycnal upwelling transport in the BBL of $\mathcal{E}_{\text{BBL}} = 60 \text{ mSv}$,
 614 where $\mathcal{E} = \frac{1}{\Delta b} \int_{\mathcal{V}(|b-b'| < \Delta b/2)} \nabla \cdot (\kappa \nabla b') dV$ is the average watermass transformation rate within
 615 a volume \mathcal{V} for a layer of thickness Δb and \mathcal{E}_{BBL} confines this integral strictly to regions
 616 of buoyancy flux convergence (see the companion manuscript Drake et al.). The upwelling
 617 transport suggested by the bulk buoyancy budget presented here (Figure 8f) is smaller than
 618 \mathcal{E}_{BBL} by a factor of three due to substantial cancellation from temporal averaging and oppos-
 619 ing cross-slope flows at the same height above the mean slope (e.g. Figure 4a). Extrapolating
 620 these BBL watermass transformations to the length of the Mid-Atlantic Ridge in the Brazil
 621 Basin (about 55 times the domain width $L_y = 60 \text{ km}$), this 3.3 Sv of BBL upwelling⁹ would
 622 alone balance much of the 3.7–4.0 Sv net inflow of Antarctic Bottom Water in the Brazil
 623 Basin (Hogg et al. 1982; Morris et al. 2001). Extrapolating even further to a global mid-

⁸Given the uncertainties of the microstructure methods, agreement within a factor of 2 is generally considered to be good (e.g. Gregg et al. 2018).

⁹This is much larger than Ruan and Callies' (2020) estimate of 0.5 Sv because our near-bottom stratification on the ridge flanks is much stronger than theirs, due to a combination of restratification effect of abyssal hills and fundamental differences between the slope-aligned and transient model configurations (see Peterson and Callies 2021).

624 ocean ridge system of length 80×10^3 km (including both flanks of the ridge; Thurnherr
625 et al. 2005) leads to a global BBL upwelling of 80 Sv due to upwelling along mid-ocean
626 ridges, roughly consistent with global diagnostic estimates of BBL upwelling (Ferrari et al.
627 2016; McDougall and Ferrari 2017).

628 Global extrapolations of localized estimates of BBL upwelling, such as the above, have
629 been used to attribute the *net* abyssal overturning to individual mixing hotspots (e.g. Ferron
630 et al. 1998; Voet et al. 2015; Thurnherr et al. 2020; Spingys et al. 2021). These observa-
631 tions, however, generally also imply significant downwelling in adjacent buoyancy classes,
632 suggesting that their localized upwelling may be offset by a similar dynamical process oper-
633 ating nearby—but centered on a different buoyancy surface. For example, Thurnherr et al.
634 (2020) argue that the observed turbulent buoyancy flux convergence in the BBTRE canyon,
635 extrapolated to all of the fracture zone canyons in the Brazil Basin, is sufficient to transform
636 “the total inflow of AABW”. Above the canyon, however, their own observations imply an
637 opposing buoyancy flux divergence of comparable magnitude; upwelling within the canyon
638 is thus only half of the story. Consider the following heuristic argument which applies the
639 slope-aligned buoyancy budgets derived in Section 2c in buoyancy coordinates. Following
640 the $\gamma_n \in \{28.1, 28.15\}$ kg/m³ neutral density class in Thurnherr et al.’s (2020) Figure 3, for
641 example, we apply eq. (16) to their integrated buoyancy fluxes in Figure 7 to infer a bulk
642 upwelling of $\Psi(z_{\text{crest}}) \simeq \frac{\langle wb \rangle / L_x}{N^2 \sin \theta} \simeq \frac{\Gamma \int \epsilon \, dy}{N^2 \sin \theta} \approx \frac{0.2 (2 \times 10^{-5} \text{ m}^3/\text{s}^3)}{(1 \times 10^{-6} \text{ s}^{-2})(2 \times 10^{-3})} = 10 \text{ mSv}$ within the canyon
643 at the DoMORE site¹⁰. This confirms Thurnherr et al.’s (2020) central conclusion that—
644 regardless of the shape of individual buoyancy flux profiles—the concave canyon topography
645 implies that the *integrated* flux peaks at the crest of the canyon and thus drives a substan-
646 tial bulk upwelling within the canyon. A few hundred km down-canyon, however, this same

¹⁰Averaging the overflow and non-overflow profiles, for simplicity.

647 density class rests above the canyon and experiences a net buoyancy flux divergence, driving
 648 a downwelling of $\Psi(z_{\text{crest}} + 500 \text{ m}) - \Psi(z_{\text{crest}}) \approx -4 \text{ mSv}$ that partially compensates for the
 649 upwelling in the canyon and suggests a significantly weaker *net* upwelling of 6 mSv for the
 650 BBTRE canyon. This heuristic exercise serves as a cautionary tale for attributing abyssal
 651 upwelling to individual regions or processes: both strictly positive and strictly negative com-
 652 ponents of watermass transformations along a buoyancy surface must be accounted for to
 653 robustly characterize the net overturning circulation.

654 At a global scale, diagnostic estimates of watermass transformations suggest significant
 655 compensation is the norm, exhibiting typical amplification factors of $\mathcal{A} \equiv \mathcal{E}_{\text{BBL}}/\mathcal{E}$ of 2 to
 656 5, where $\mathcal{E} = \mathcal{E}_{\text{BBL}} + \mathcal{E}_{\text{SML}}$ is the net diapycnal transport and \mathcal{E}_{SML} is the downwelling in
 657 the stratified mixing layer (Ferrari et al. 2016; McDougall and Ferrari 2017; Cimoli et al.
 658 2019). However, these diagnostic exercises do not provide any insight into the physics
 659 underlying the observed density structure that supports these transformations. More prob-
 660 lematically, these results seem to contradict the weak upwelling with $\mathcal{A} \simeq 1$ implied by 1D
 661 boundary layer dynamics (Section 2b). Building upon Callies (2018) and Ruan and Callies
 662 (2020), our prognostic modelling approach demonstrates how three-dimensional eddy and
 663 topographic effects conspire to provide sufficient restratification to support a significant up-
 664 welling/downwelling dipole, i.e. $\mathcal{A} \gg 1$ (Figure 8a,f). Our results inspire two open questions:
 665 1) which topographic regimes (e.g. ridges, slopes, plains) or topographic roughness features
 666 (e.g. hills, canyons, channels, sills, or seamounts) contribute the most to abyssal watermass
 667 transformations (e.g. Armi and D’Asaro 1980; Bryden and Nurser 2003; Thurnherr et al.
 668 2005; Legg et al. 2009; Nazarian et al. 2021; Mashayek et al. 2021) and 2) what are the dy-
 669 namics that support finite watermass transformations in these regions (Garrett 1979, 1990;
 670 Callies 2018; Drake et al. 2020)?

671 Our combined assumptions of constant background stratification and zero barotropic cross-
672 slope pressure gradient assert that the net upwelling scales with the background diffusivity
673 (eq. 13) and thus that the net upwelling $\Psi_\infty = \mathcal{E}$ is very small. While our local model helps
674 explain the magnitude of bottom boundary layer upwelling \mathcal{E}_{BBL} , it does not meaningfully
675 constrain \mathcal{E}_{SML} or \mathcal{A} . Salmun et al. (1991) use asymptotic analysis to show that small
676 perturbations away from a constant interior stratification drive an exchange flow between
677 the boundary and the interior, which then feeds back on the interior stratification. In the
678 context of the abyssal ocean, vertical variations in the basin-scale interior stratification are
679 relatively large, such that they enter as leading-order terms in watermass transformations
680 (Spingys et al. 2021) and drive substantial exchange between the mixing layers and the
681 interior (Holmes et al. 2018). In Drake et al.’s (2020) idealized basin-scale simulations,
682 this boundary–interior coupling results in a substantial reduction of \mathcal{E}_{SML} , permitting an
683 amplification factor of $\mathcal{A} = 1.5$ much smaller than the $\mathcal{A} \gg 1$ governed by local dynamics.
684 These idealized prognostic model results are qualitatively consistent with the diagnostic
685 approaches described above, but quantitative understanding of \mathcal{E}_{BBL} , \mathcal{E}_{SML} , and \mathcal{A} remains
686 incomplete.

687 Understanding of bottom-enhanced mixing has advanced considerably in recent years due
688 to a combination of breakthroughs in observation (e.g. Polzin et al. 1997; Ledwell et al.
689 2000), theory (e.g. Polzin 2009), and modelling (e.g. Nikurashin and Legg 2011). The
690 interpretation of these results in terms of broad diapycnal downwelling in the SML atop
691 vigorous diapycnal upwelling in a BBL (Ferrari et al. 2016), however, is challenged by higher-
692 resolution observations (van Haren 2018; Naveira Garabato et al. 2019; Polzin et al. 2021)
693 and simulations (Gayen and Sarkar 2011; Kaiser 2020) of mixing processes within the bottom
694 few dozen meters of the ocean. In addition to the debate on the nature of boundary mixing

695 itself (see Polzin and McDougall 2022), the role of the resulting boundary layer flows in the
696 global overturning circulation remains shrouded by poor understanding of their coupling to
697 the far-field interior (Drake et al. 2020; Peterson and Callies 2021).

698 *Acknowledgments.* We thank the crews of the BBTRE and DoMORE field campaigns for
699 collecting the observations that motivated this work. We acknowledge funding support from
700 National Science Foundation Awards 6932401 and 6936732. This material is based upon
701 work supported by the National Science Foundation Graduate Research Fellowship Program
702 under Grant No. 174530. Any opinions, findings, and conclusions or recommendations
703 expressed in this material are those of the author(s) and do not necessarily reflect the
704 views of the National Science Foundation. This research is also supported by the NOAA
705 Climate and Global Change Postdoctoral Fellowship Program, administered by UCAR’s
706 Cooperative Programs for the Advancement of Earth System Science (CPAESS) under award
707 #NA18NWS4620043B.

708 *Data availability statement.* The source code for the MITgcm simulations and all of the
709 Python code necessary to produce the figures will be publicly available at [github.com/
710 hdrake/sim-bbtre](https://github.com/hdrake/sim-bbtre) upon acceptance (or earlier by requesting the corresponding author).
711 Our analysis of labeled data arrays is greatly simplified by the `xarray` package in Python
712 (Hoyer and Hamman 2017).

713 APPENDIX

714 **One-dimensional model of restratification by submesoscale baroclinic eddies** 715 **along a sloping boundary**

716 Our goal is to reformulate the 1D sloping BBL model using Transformed Eulerian Mean
717 (TEM) theory (Andrews and McIntyre 1976) to facilitate the inclusion of submesoscale eddy
718 restratification. We begin by assuming there are no large-scale variations in the perturba-
719 tions, so that we can average in the along-slope (y) and cross-slope (x) directions and drop
720 cross- and along-slope gradients. Then, averaging the slope-aligned equations (1–5) in both
721 x and y , we have

$$\bar{u}_t - f\bar{v} \cos \theta - \bar{b} \sin \theta - \partial_z (\kappa \bar{u}_z) = -\partial_z (\overline{w'u'}), \quad (\text{A1})$$

$$\bar{v}_t + f\bar{u} \cos \theta - \partial_z (\kappa \bar{v}_z) = -\partial_z (\overline{w'v'}), \quad (\text{A2})$$

$$\bar{p}_z - \bar{b} \cos \theta = 0, \quad (\text{A3})$$

$$\bar{b}_t + \bar{u} N^2 \sin \theta - \partial_z (\kappa \bar{B}_z) = -\partial_z (\overline{w'b'}), \quad (\text{A4})$$

722 where the eddy fluctuations $\phi' \equiv \phi - \bar{\phi}$ are departures from the slope-average means $\bar{\phi}$,
723 $\bar{w} = 0$ from continuity and the no-flux bottom boundary condition, and we assume $\sigma = 1$.

724 We introduce the residual velocities

$$(u^\dagger, w^\dagger) \equiv (\bar{u}, \bar{w}) + (-\partial_z, \partial_x) \psi_e, \quad (\text{A5})$$

725 which add to the Eulerian mean flow $\bar{\mathbf{u}}$ an eddy-induced overturning $\nabla \times \mathbf{y}\psi_e$ in the (x, z)
726 plane that is by definition also non-divergent.

727 Using a convenient definition of the eddy streamfunction—Plumb and Ferrari (2005) show
728 that its definition is not unique—inspired by Andrews and McIntyre (1976) but in a rotated
729 coordinate frame,

$$\psi_e \equiv \frac{\overline{u'b'}}{\bar{B}_z}, \quad (\text{A6})$$

730 we express the slope-averaged equations (A1–A4) in terms of the residual circulation $\mathbf{u}^\dagger =$
731 $(u^\dagger, \bar{v}, w^\dagger)$. Since, by assumption, the large-scale average solution is independent of x , we

732 have $\partial_x \psi_e = 0$ and thus $w^\dagger = \bar{w} = 0$. With this choice of eddy streamfunction (A6) and
 733 associated residual velocity, the momentum and buoyancy budget take the form,

$$\bar{v}_t + f u^\dagger \cos \theta - \partial_z (\kappa \bar{v}_z) = -\partial_z \left(\overline{w'v'} + f \cos \theta \frac{\overline{u'b'}}{\bar{B}_z} \right), \quad (\text{A7})$$

$$\bar{b}_t + u^\dagger N^2 \sin \theta - \partial_z (\kappa \bar{B}_z) = -\partial_z \left[\frac{\overline{\mathbf{u}'b' \cdot \nabla B}}{\bar{B}_z} \right], \quad (\text{A8})$$

734 where we recall the total buoyancy is decomposed as $B \equiv N^2 \hat{z} + \bar{b} + b'$. The main advantage
 735 of working in terms of residual velocity is that only the eddy flux terms normal to density
 736 surfaces appears in the buoyancy budget. The mean slope of isopycnals in the rotated
 737 reference frame is given by $-\bar{B}_x/\bar{B}_z = -N^2 \sin \theta / (N^2 \cos \theta + \bar{b}_z)$ because \bar{b} is independent
 738 of x . Thus $\overline{\mathbf{u}'b' \cdot \nabla B}$ is the dot product of the eddy buoyancy flux with the mean buoyancy
 739 gradient, which is punishingly small because the submesoscale eddies are characterized by
 740 large Richardson numbers and do not generate mixing across density surfaces, as illustrated
 741 in Figure 11b for our numerical solutions. Then, at leading order,

$$\bar{b}_t + u^\dagger N^2 \sin \theta - \partial_z (\kappa \bar{B}_z) = 0, \quad (\text{A9})$$

742 and the eddy closure problem is confined to the residual along-slope momentum flux (A7).
 743 This is the main advantage of working in terms of residual velocity, \mathbf{u}^\dagger , instead of Eulerian
 744 mean velocity. The residual velocity is the mean Lagrangian velocity that advects tracers,
 745 without additional contributions from eddy fluxes as can be seen in equation (A9).

746 Assuming quasi-geostrophic scaling for the eddy fluxes, the Reynolds flux term in (A7)
 747 is $\mathcal{O}(R_o)$ smaller than the buoyancy flux term and can be neglected. Closing the system
 748 then only requires a closure for the cross-slope eddy buoyancy flux $\overline{u'b'}$ that appears in the
 749 y -momentum equation. Following the argument proposed by Gent and McWilliams (1990);
 750 Gent et al. (1995), i.e. that quasi-geostrophic eddies generated through baroclinic instability
 751 act to flatten isopycnals and thus release available potential energy, we assume that the truly

752 horizontal buoyancy flux is down-gradient,

$$\overline{\hat{w}'b'} \simeq -K(z)\overline{B_{\hat{x}}}. \quad (\text{A10})$$

753 This closure can be expressed in slope coordinates, $\overline{B_{\hat{x}}} = -\overline{b}_z \sin \theta$, such that

$$K(z) = -\frac{\overline{\hat{w}'b'}}{\overline{B_{\hat{x}}}} = -\frac{\overline{u'b'} \cos \theta - \overline{w'b'} \sin \theta}{-\overline{b}_z \sin \theta} = \frac{\overline{u'b'}}{\overline{B}_z} \frac{N^2 + \overline{b}_z \cos \theta}{\overline{b}_z \sin \theta}, \quad (\text{A11})$$

754 where we used the fact that the flux normal to density surfaces vanish and thus $\overline{w'b'} =$
 755 $-\overline{u'b'} \overline{B}_x / \overline{B}_z$. It is worth noting that $\overline{B}_z = N^2 + \overline{b}_z \cos \theta$ is the true-vertical buoyancy
 756 gradient.

757 To clarify the role of this additional eddy-induced overturning, we focus on the stratified
 758 interior above the frictional bottom layer, where geostrophic balance applies to the mean
 759 along-slope flow in the mean cross-slope (\mathbf{x}) momentum equation (as in semi-geostrophic
 760 theories of frontogenesis),

$$-f\overline{v}_z \cos \theta = \overline{b}_z \sin \theta. \quad (\text{A12})$$

761 Combining (A11) and (A12) and plugging back into (A7) yields

$$\overline{v}_t + fu^\dagger \cos \theta = \partial_z (\nu_e(z)\overline{v}_z), \quad (\text{A13})$$

762 where we defined

$$\nu_e(z) \equiv \sigma_v(z)\kappa(z) \quad \text{with} \quad \sigma_v(z) \equiv 1 + \frac{K(z)}{\kappa(z)} \frac{f^2}{\overline{B}_z} \cos^2 \theta \quad (\text{A14})$$

763 as an enhanced vertical momentum diffusion (as in Greatbatch and Lamb 1990 but modified
 764 by the geometric factor $\cos^2 \theta$, which approaches unity for shallow slopes).

765 Although we have shown that the slope-averaged equations can be closed through an en-
 766 hanced eddy viscosity, the parameterization is incomplete since we have not specified the
 767 magnitude or structure of $K(z)$ in terms of only resolved quantities and external parameters.

768 Developing such a parameterization is beyond the scope of this paper; however, we can ex-
 769 plore the impact of such a parameterization by diagnosing the cross-slope eddy flux—and the
 770 resulting effective eddy diffusivity (A11)—from the Smooth3D simulation and substituting
 771 it back into the corresponding 1D model given by

$$u_t^\dagger - f\bar{v} \cos \theta = \bar{b} \sin \theta + \partial_z (\kappa u_z^\dagger), \quad (\text{A15})$$

$$\bar{v}_t + f u^\dagger \cos \theta = \partial_z (\sigma_v(z) \kappa \bar{v}_z), \quad (\text{A16})$$

$$w^\dagger = 0 \quad (\text{A17})$$

$$\bar{p}_z = \bar{b} \cos \theta, \quad (\text{A18})$$

$$\bar{b}_t + u^\dagger N^2 \sin \theta = \partial_z [\kappa (N^2 \cos \theta + \bar{b}_z)]. \quad (\text{A19})$$

772 This set of equations is identical to the canonical 1D sloping BBL model (8) through (10)
 773 for the Eulerian mean circulation except for the enhancement of vertical diffusion of along-
 774 slope momentum by a factor $\sigma_v(z)$. Figure 11a shows how the effective vertical Prandtl
 775 number can be approximated by a simple vertical structure, $\sigma_v(z) \propto z \exp\{-z/\eta\}$ with an
 776 optimal vertical scale of $\eta = 225 \text{ m} \approx h$ and a peak magnitude of $\sigma_v = \mathcal{O}(100)$, dramatically
 777 enhancing the vertical diffusion of the along-slope thermal wind. This form satisfies $\sigma_v \rightarrow 1$
 778 as $z \rightarrow 0$, such that the eddy-induced flow does not interfere with the bottom boundary
 779 conditions on the Eulerian mean flow.

780 Figure 1 and Figures 8a,b,c show the impact of this momentum diffusion on the 1D BBL
 781 solution and its buoyancy budget, respectively. Callies (2018) and Holmes et al. (2019) pro-
 782 pose conceptually similar parameterizations, but omit the derivation and assume a vertically-
 783 uniform enhancement of the Prandtl number $\sigma = 230$, which distorts the vertical structure
 784 of submesoscale eddy restratification.

785 **References**

- 786 Andrews, D. G., and M. E. McIntyre, 1976: Planetary Waves in Horizontal and Vertical
787 Shear: The Generalized Eliassen-Palm Relation and the Mean Zonal Acceleration. *Journal*
788 *of the Atmospheric Sciences*, **33 (11)**, 2031–2048, doi:10.1175/1520-0469(1976)033<2031:
789 PWIHAV>2.0.CO;2, publisher: American Meteorological Society.
- 790 Armi, L., 1978: Some evidence for boundary mixing in the deep Ocean. *Journal of Geophys-*
791 *ical Research*, **83 (C4)**, 1971, doi:10.1029/JC083iC04p01971, URL [http://doi.wiley.com/](http://doi.wiley.com/10.1029/JC083iC04p01971)
792 [10.1029/JC083iC04p01971](http://doi.wiley.com/10.1029/JC083iC04p01971).
- 793 Armi, L., 1979a: Effects of variations in eddy diffusivity on property distributions in the
794 oceans. *Journal of Marine Research*, **37 (3)**, 515–530, URL [https://escholarship.org/uc/](https://escholarship.org/uc/item/65g216cr)
795 [item/65g216cr](https://escholarship.org/uc/item/65g216cr).
- 796 Armi, L., 1979b: Reply to Comments by C. Garrett. *Journal of Geophysical Re-*
797 *search*, **84 (C8)**, 5097, doi:10.1029/JC084iC08p05097, URL [http://doi.wiley.com/10.](http://doi.wiley.com/10.1029/JC084iC08p05097)
798 [1029/JC084iC08p05097](http://doi.wiley.com/10.1029/JC084iC08p05097), publisher: Wiley-Blackwell.
- 799 Armi, L., and E. D’Asaro, 1980: Flow structures of the benthic ocean. *Journal of Geophysi-*
800 *cal Research: Oceans*, **85 (C1)**, 469–484, doi:<https://doi.org/10.1029/JC085iC01p00469>,
801 URL <https://agupubs.onlinelibrary.wiley.com/doi/abs/10.1029/JC085iC01p00469>,
802 [_eprint: https://agupubs.onlinelibrary.wiley.com/doi/pdf/10.1029/JC085iC01p00469](https://agupubs.onlinelibrary.wiley.com/doi/pdf/10.1029/JC085iC01p00469).
- 803 Baines, P. G., 1979: Observations of stratified flow past Three-dimensional barriers. *Journal*
804 *of Geophysical Research: Oceans*, **84 (C12)**, 7834–7838, doi:10.1029/JC084iC12p07834,
805 URL <https://agupubs.onlinelibrary.wiley.com/doi/abs/10.1029/JC084iC12p07834>,
806 [_eprint: https://agupubs.onlinelibrary.wiley.com/doi/pdf/10.1029/JC084iC12p07834](https://agupubs.onlinelibrary.wiley.com/doi/pdf/10.1029/JC084iC12p07834).

807 Boccaletti, G., R. Ferrari, and B. Fox-Kemper, 2007: Mixed Layer Instabilities and Restrat-
808 ification. *Journal of Physical Oceanography*, **37** (9), 2228–2250, doi:10.1175/JPO3101.1,
809 URL <http://journals.ametsoc.org/doi/abs/10.1175/JPO3101.1>.

810 Bryden, H. L., and A. J. G. Nurser, 2003: Effects of Strait Mixing on Ocean Stratifica-
811 tion. *Journal of Physical Oceanography*, **33** (8), 1870–1872, doi:10.1175/1520-0485(2003)
812 033(1870:EOSMOO)2.0.CO;2, URL [https://journals.ametsoc.org/view/journals/phoc/
813 33/8/1520-0485_2003_033_1870_eosmoo_2.0.co_2.xml](https://journals.ametsoc.org/view/journals/phoc/33/8/1520-0485_2003_033_1870_eosmoo_2.0.co_2.xml), publisher: American Meteorological
814 Society Section: Journal of Physical Oceanography.

815 Burns, K. J., G. M. Vasil, J. S. Oishi, D. Lecoanet, and B. Brown, 2016: Dedalus: Flexible
816 framework for spectrally solving differential equations. *Astrophysics Source Code Library*,
817 *record ascl:1603.015*, URL <http://adsabs.harvard.edu/abs/2016ascl.soft03015B>.

818 Cael, B., and A. Mashayek, 2021: Log-Skew-Normality of Ocean Turbulence. *Physical*
819 *Review Letters*, **126** (22), 224502, doi:10.1103/PhysRevLett.126.224502, URL [https:
820 //link.aps.org/doi/10.1103/PhysRevLett.126.224502](https://link.aps.org/doi/10.1103/PhysRevLett.126.224502), publisher: American Physical So-
821 ciety.

822 Callies, J., 2018: Restratification of Abyssal Mixing Layers by Submesoscale Baroclinic Ed-
823 dies. *Journal of Physical Oceanography*, JPO–D–18–0082.1, doi:10.1175/JPO-D-18-0082.
824 1, URL <http://journals.ametsoc.org/doi/10.1175/JPO-D-18-0082.1>.

825 Callies, J., and R. Ferrari, 2018: Dynamics of an Abyssal Circulation Driven by Bottom-
826 Intensified Mixing on Slopes. *Journal of Physical Oceanography*, **48** (6), 1257–1282, doi:10.
827 1175/JPO-D-17-0125.1, URL [http://journals.ametsoc.org/doi/10.1175/JPO-D-17-0125.
828 1](http://journals.ametsoc.org/doi/10.1175/JPO-D-17-0125.1).

829 Cimoli, L., C.-c. P. Caulfield, H. L. Johnson, D. P. Marshall, A. Mashayek, A. C. N. Gara-
830 bato, and C. Vic, 2019: Sensitivity of deep ocean mixing to local internal tide breaking and
831 mixing efficiency. *Geophysical Research Letters*, **n/a (n/a)**, doi:10.1029/2019GL085056,
832 URL <https://agupubs.onlinelibrary.wiley.com/doi/abs/10.1029/2019GL085056>.

833 Clément, L., A. M. Thurnherr, and L. C. St. Laurent, 2017: Turbulent Mixing in a
834 Deep Fracture Zone on the Mid-Atlantic Ridge. *Journal of Physical Oceanography*,
835 **47 (8)**, 1873–1896, doi:10.1175/JPO-D-16-0264.1, URL <http://journals.ametsoc.org/doi/10.1175/JPO-D-16-0264.1>.

837 de Lavergne, C., G. Madec, J. Le Sommer, A. J. G. Nurser, and A. C. Naveira Garabato,
838 2016: On the Consumption of Antarctic Bottom Water in the Abyssal Ocean. *Journal*
839 *of Physical Oceanography*, **46 (2)**, 635–661, doi:10.1175/JPO-D-14-0201.1, URL <http://journals.ametsoc.org/doi/10.1175/JPO-D-14-0201.1>.

841 de Lavergne, C., and Coauthors, 2020: A Parameterization of Local and
842 Remote Tidal Mixing. *Journal of Advances in Modeling Earth Systems*,
843 **12 (5)**, e2020MS002065, doi:<https://doi.org/10.1029/2020MS002065>, URL
844 <https://agupubs.onlinelibrary.wiley.com/doi/abs/10.1029/2020MS002065>, eprint:
845 <https://agupubs.onlinelibrary.wiley.com/doi/pdf/10.1029/2020MS002065>.

846 Dell, R., and L. Pratt, 2015: Diffusive boundary layers over varying topography. *Journal*
847 *of Fluid Mechanics*, **769**, 635–653, doi:10.1017/jfm.2015.88, URL http://www.journals.cambridge.org/abstract_S0022112015000889.

849 Dell, R. W., 2013: *Boundary layer dynamics and deep ocean mixing in Mid-Atlantic Ridge*
850 *canyons*. Massachusetts Institute of Technology and Woods Hole Oceanographic Institu-
851 tion, Woods Hole, MA, doi:10.1575/1912/5740, URL <https://hdl.handle.net/1912/5740>.

852 Drake, H. F., 2021: Control of the abyssal ocean overturning circulation by mixing-
853 driven bottom boundary layers. Thesis, Massachusetts Institute of Technology and
854 Woods Hole Oceanographic Institution, doi:10.1575/1912/27424, URL <https://darchive.mblwhoilibrary.org/handle/1912/27424>, accepted: 2021-08-10T15:07:15Z.

856 Drake, H. F., R. Ferrari, and J. Callies, 2020: Abyssal Circulation Driven
857 by Near-Boundary Mixing: Water Mass Transformations and Interior Strat-
858 ification. *Journal of Physical Oceanography*, **50** (8), 2203–2226, doi:10.1175/
859 JPO-D-19-0313.1, URL [https://journals.ametsoc.org/jpo/article/50/8/2203/348530/
860 Abyssal-Circulation-Driven-by-Near-Boundary-Mixing](https://journals.ametsoc.org/jpo/article/50/8/2203/348530/Abyssal-Circulation-Driven-by-Near-Boundary-Mixing), publisher: American Meteorolog-
861 ical Society.

862 Ferrari, R., 2014: What goes down must come up. *Nature*, **513**, 179–180.

863 Ferrari, R., A. Mashayek, T. J. McDougall, M. Nikurashin, and J.-M. Campin, 2016: Turning
864 Ocean Mixing Upside Down. *Journal of Physical Oceanography*, **46** (7), 2239–2261, doi:10.
865 1175/JPO-D-15-0244.1, URL [http://journals.ametsoc.org/doi/10.1175/JPO-D-15-0244.
866 1](http://journals.ametsoc.org/doi/10.1175/JPO-D-15-0244.1).

867 Ferrari, R., and R. Plumb, 2003: Residual circulation in the ocean. *Near-Boundary Processes
868 and Their Parameterization: Proc. 'Aha Huliko'a Hawaiian Winter Workshop*, 219–228.

869 Ferron, B., H. Mercier, K. Speer, A. Gargett, and K. Polzin, 1998: Mixing in the Romanche
870 Fracture Zone. *Journal of Physical Oceanography*, **28** (10), 1929–1945, doi:10.1175/
871 1520-0485(1998)028<1929:MITRFZ>2.0.CO;2, URL [https://journals.ametsoc.org/view/
872 journals/phoc/28/10/1520-0485_1998_028_1929_mitr fz_2.0.co_2.xml](https://journals.ametsoc.org/view/journals/phoc/28/10/1520-0485_1998_028_1929_mitr fz_2.0.co_2.xml), publisher: American
873 Meteorological Society Section: Journal of Physical Oceanography.

874 Fox-Kemper, B., R. Ferrari, and R. Hallberg, 2008: Parameterization of Mixed Layer Ed-
875 dies. Part I: Theory and Diagnosis. *Journal of Physical Oceanography*, **38** (6), 1145–
876 1165, doi:10.1175/2007JPO3792.1, URL [http://journals.ametsoc.org/doi/abs/10.1175/
877 2007JPO3792.1](http://journals.ametsoc.org/doi/abs/10.1175/2007JPO3792.1).

878 Garrett, C., 1979: Comment on ‘Some evidence for boundary mixing in the deep
879 ocean’ by Laurence Armi. *Journal of Geophysical Research*, **84** (C8), 5095, doi:
880 10.1029/JC084iC08p05095, URL <http://doi.wiley.com/10.1029/JC084iC08p05095>, pub-
881 lisher: Wiley-Blackwell.

882 Garrett, C., 1990: The role of secondary circulation in boundary mixing. *Journal of Geo-
883 physical Research*, **95** (C3), 3181, doi:10.1029/JC095iC03p03181, URL [http://doi.wiley.
884 com/10.1029/JC095iC03p03181](http://doi.wiley.com/10.1029/JC095iC03p03181), publisher: Wiley-Blackwell.

885 Garrett, C., P. MacCready, and P. Rhines, 1993: Boundary Mixing and Arrested Ekman
886 Layers: Rotating Stratified Flow Near a Sloping Boundary. *Annual Review of Fluid Me-
887 chanics*, **25** (1), 291–323, doi:10.1146/annurev.fl.25.010193.001451, URL [http://www.
888 annualreviews.org/doi/10.1146/annurev.fl.25.010193.001451](http://www.annualreviews.org/doi/10.1146/annurev.fl.25.010193.001451), publisher: Annual Reviews
889 4139 El Camino Way, P.O. Box 10139, Palo Alto, CA 94303-0139, USA.

890 Gayen, B., and S. Sarkar, 2011: Negative turbulent production during flow reversal in a strat-
891 ified oscillating boundary layer on a sloping bottom. *Physics of Fluids*, **23** (10), 101703,
892 doi:10.1063/1.3651359, URL <https://aip.scitation.org/doi/10.1063/1.3651359>, publisher:
893 American Institute of Physics.

894 Gent, P. R., and J. C. McWilliams, 1990: Isopycnal Mixing in Ocean Cir-
895 culation Models. *Journal of Physical Oceanography*, **20** (1), 150–155, doi:10.

896 1175/1520-0485(1990)020<0150:IMIOCM>2.0.CO;2, URL [http://journals.ametsoc.org/doi/abs/10.1175/1520-0485\(1990\)020%3C0150:IMIOCM%3E2.0.CO;2](http://journals.ametsoc.org/doi/abs/10.1175/1520-0485(1990)020%3C0150:IMIOCM%3E2.0.CO;2), iSBN: 0022-3670.

898 Gent, P. R., J. Willebrand, T. J. McDougall, and J. C. McWilliams, 1995: Parameter-
899 izing Eddy-Induced Tracer Transports in Ocean Circulation Models. *Journal of Phys-*
900 *ical Oceanography*, **25** (4), 463–474, doi:10.1175/1520-0485(1995)025<0463:PEITTI>2.0.
901 CO;2, URL [https://journals.ametsoc.org/view/journals/phoc/25/4/1520-0485_1995_025_](https://journals.ametsoc.org/view/journals/phoc/25/4/1520-0485_1995_025_0463_peitti_2_0_co_2.xml)
902 [0463_peitti_2_0_co_2.xml](https://journals.ametsoc.org/view/journals/phoc/25/4/1520-0485_1995_025_0463_peitti_2_0_co_2.xml), publisher: American Meteorological Society Section: Journal of
903 Physical Oceanography.

904 Gordon, A. L., 1986: Is there a global scale ocean circulation? *Eos, Transactions American*
905 *Geophysical Union*, **67** (9), 109–110, doi:<https://doi.org/10.1029/EO067i009p00109>,
906 URL <https://agupubs.onlinelibrary.wiley.com/doi/abs/10.1029/EO067i009p00109>,
907 [_eprint: https://agupubs.onlinelibrary.wiley.com/doi/pdf/10.1029/EO067i009p00109](https://agupubs.onlinelibrary.wiley.com/doi/pdf/10.1029/EO067i009p00109).

908 Greatbatch, R. J., and K. G. Lamb, 1990: On Parameterizing Vertical Mixing of
909 Momentum in Non-eddy Resolving Ocean Models. *Journal of Physical Oceanog-*
910 *raphy*, **20** (10), 1634–1637, doi:10.1175/1520-0485(1990)020<1634:OPVMOM>2.0.
911 CO;2, URL [https://journals.ametsoc.org/doi/abs/10.1175/1520-0485%281990%29020%](https://journals.ametsoc.org/doi/abs/10.1175/1520-0485%281990%29020%3C1634%3AOPVMOM%3E2.0.CO%3B2)
912 [3C1634%3AOPVMOM%3E2.0.CO%3B2](https://journals.ametsoc.org/doi/abs/10.1175/1520-0485%281990%29020%3C1634%3AOPVMOM%3E2.0.CO%3B2).

913 Gregg, M., E. D’Asaro, J. Riley, and E. Kunze, 2018: Mixing Efficiency in the Ocean. *Annual*
914 *Review of Marine Science*, **10** (1), 443–473, doi:10.1146/annurev-marine-121916-063643,
915 URL <http://www.annualreviews.org/doi/10.1146/annurev-marine-121916-063643>.

916 Gregg, M. C., 1987: Diapycnal mixing in the thermocline: A review. *Journal of Geophysical*
917 *Research*, **92** (C5), 5249, doi:10.1029/JC092iC05p05249, URL [http://doi.wiley.com/10.](http://doi.wiley.com/10.1029/JC092iC05p05249)
918 [1029/JC092iC05p05249](http://doi.wiley.com/10.1029/JC092iC05p05249).

919 Held, I. M., 2005: The gap between simulation and understanding in climate model-
920 ing. *Bulletin of the American Meteorological Society*, **86 (11)**, 1609–1614, doi:10.1175/
921 BAMS-86-11-1609, iISBN: 0003-0007.

922 Hogg, N., P. Biscaye, W. Gardner, and W. Jr, 1982: On the Transport and Modification of
923 Antarctic Bottom Water in the Vema Channel. *J. Mar. Res.*, **40**, 231–263.

924 Holmes, R. M., C. de Lavergne, and T. J. McDougall, 2018: Ridges, Seamounts, Troughs,
925 and Bowls: Topographic Control of the Diapycnal Circulation in the Abyssal Ocean.
926 *Journal of Physical Oceanography*, **48 (4)**, 861–882, doi:10.1175/JPO-D-17-0141.1, URL
927 <http://journals.ametsoc.org/doi/10.1175/JPO-D-17-0141.1>.

928 Holmes, R. M., C. de Lavergne, and T. J. McDougall, 2019: Tracer Transport within Abyssal
929 Mixing Layers. *Journal of Physical Oceanography*, **49 (10)**, 2669–2695, doi:10.1175/
930 JPO-D-19-0006.1, URL [https://journals.ametsoc.org/doi/full/10.1175/JPO-D-19-0006.](https://journals.ametsoc.org/doi/full/10.1175/JPO-D-19-0006.1)
931 1, publisher: American Meteorological Society.

932 Holmes, R. M., and T. J. McDougall, 2020: Diapycnal Transport near a Sloping
933 Bottom Boundary. *Journal of Physical Oceanography*, **50 (11)**, 3253–3266, doi:10.
934 1175/JPO-D-20-0066.1, URL [https://journals.ametsoc.org/view/journals/phoc/50/11/
935 jpoD200066.xml](https://journals.ametsoc.org/view/journals/phoc/50/11/jpoD200066.xml), publisher: American Meteorological Society Section: Journal of Physical
936 Oceanography.

937 Hoyer, S., and J. Hamman, 2017: xarray: N-D labeled arrays and datasets in Python.
938 *Journal of Open Research Software*, **5 (1)**, doi:10.5334/jors.148, URL [http://doi.org/10.
939 5334/jors.148](http://doi.org/10.5334/jors.148).

- 940 Huang, R. X., and X. Jin, 2002: Deep Circulation in the South Atlantic Induced by Bottom-
941 Intensified Mixing over the Midocean Ridge*. *Journal of Physical Oceanography*, **32** (4),
942 1150–1164, doi:10.1175/1520-0485(2002)032<1150:DCITSA>2.0.CO;2.
- 943 Ijichi, T., L. S. Laurent, K. L. Polzin, and J. M. Toole, 2020: How
944 Variable Is Mixing Efficiency in the Abyss? *Geophysical Research Let-*
945 *ters*, **47** (7), e2019GL086813, doi:10.1029/2019GL086813, URL <https://agupubs.onlinelibrary.wiley.com/doi/abs/10.1029/2019GL086813>,
946 [_eprint: https://agupubs.onlinelibrary.wiley.com/doi/pdf/10.1029/2019GL086813](https://agupubs.onlinelibrary.wiley.com/doi/pdf/10.1029/2019GL086813).
- 947
- 948 Kaiser, B. E., 2020: Finescale abyssal turbulence : sources and modeling. Thesis, Mas-
949 sachusetts Institute of Technology, URL <https://dspace.mit.edu/handle/1721.1/128078>,
950 accepted: 2020-10-18T21:45:36Z.
- 951 Kunze, E., 2017: The Internal-Wave-Driven Meridional Overturning Circulation. *Journal*
952 *of Physical Oceanography*, **47** (11), 2673–2689, doi:10.1175/JPO-D-16-0142.1, URL <http://journals.ametsoc.org/doi/10.1175/JPO-D-16-0142.1>.
- 953
- 954 Kunze, E., E. Firing, J. M. Hummon, T. K. Chereskin, and A. M. Thurnherr, 2006:
955 Global Abyssal Mixing Inferred from Lowered ADCP Shear and CTD Strain Profiles.
956 *Journal of Physical Oceanography*, **36** (8), 1553–1576, doi:10.1175/JPO2926.1, URL
957 <https://journals.ametsoc.org/view/journals/phoc/36/8/jpo2926.1.xml>, publisher: Amer-
958 ican Meteorological Society Section: Journal of Physical Oceanography.
- 959 Kunze, E., C. MacKay, E. E. McPhee-Shaw, K. Morrice, J. B. Girton, and S. R. Terker, 2012:
960 Turbulent Mixing and Exchange with Interior Waters on Sloping Boundaries. *Journal*
961 *of Physical Oceanography*, **42** (6), 910–927, doi:10.1175/JPO-D-11-075.1, URL [http://](http://journals.ametsoc.org/doi/abs/10.1175/JPO-D-11-075.1)
962 journals.ametsoc.org/doi/abs/10.1175/JPO-D-11-075.1.

- 963 Ledwell, J. R., E. T. Montgomery, K. L. Polzin, L. C. St. Laurent, R. W. Schmitt, and
964 J. M. Toole, 2000: Evidence for enhanced mixing over rough topography in the abyssal
965 ocean. *Nature*, **403 (6766)**, 179–182, doi:10.1038/35003164, URL <http://www.nature.com/articles/35003164>, publisher: Nature Publishing Group.
- 967 Ledwell, J. R., A. J. Watson, and C. S. Law, 1993: Evidence for slow mixing across the pyc-
968 nocline from an open-ocean tracer-release experiment. *Nature*, **364 (6439)**, 701–703, doi:
969 10.1038/364701a0, URL <http://www.nature.com/doi/10.1038/364701a0>, publisher:
970 Nature Publishing Group.
- 971 Legg, S., and Coauthors, 2009: Improving Oceanic Overflow Representation in Climate
972 Models: The Gravity Current Entrainment Climate Process Team. *Bulletin of the*
973 *American Meteorological Society*, **90 (5)**, 657–670, doi:10.1175/2008BAMS2667.1, URL
974 https://journals.ametsoc.org/view/journals/bams/90/5/2008bams2667_1.xml, publisher:
975 American Meteorological Society Section: Bulletin of the American Meteorological Soci-
976 ety.
- 977 MacCready, P., and P. B. Rhines, 1991: Buoyant inhibition of Ekman transport on
978 a slope and its effect on stratified spin-up. *Journal of Fluid Mechanics*, **223 (-1)**,
979 631, doi:10.1017/S0022112091001581, URL [http://www.journals.cambridge.org/abstract_](http://www.journals.cambridge.org/abstract_S0022112091001581)
980 [S0022112091001581](http://www.journals.cambridge.org/abstract_S0022112091001581), publisher: Cambridge University Press.
- 981 Marshall, J., C. Hill, L. Perelman, and A. Adcroft, 1997: Hydrostatic, quasi-hydrostatic,
982 and nonhydrostatic ocean modeling. *Journal of Geophysical Research*, **102 (C3)**, 5733,
983 doi:10.1029/96JC02776, iSBN: 2156-2202.
- 984 Marshall, J., and T. Radko, 2003: Residual-Mean Solutions for the Antarctic Cir-
985 cumpolar Current and Its Associated Overturning Circulation. *Journal of Physical*

986 *Oceanography*, **33** (11), 2341–2354, doi:10.1175/1520-0485(2003)033<2341:RSFTAC>2.
987 0.CO;2, URL [http://dx.doi.org/10.1175/1520-0485\(2003\)033%3C2341:RSFTAC%3E2.0](http://dx.doi.org/10.1175/1520-0485(2003)033%3C2341:RSFTAC%3E2.0).
988 CO;2, iISBN: 0022-3670.

989 Mashayek, A., J. Gula, L. Baker, A. N. Garabato, L. Cimoli, and J. Riley, 2021: Mountains
990 to climb: on the role of seamounts in upwelling of deep ocean water. Tech. rep. doi:10.
991 21203/rs.3.rs-939198/v1, URL <https://doi.org/10.21203/rs.3.rs-939198/v1>, type: article.

992 McDougall, T. J., and R. Ferrari, 2017: Abyssal Upwelling and Downwelling Driven by
993 Near-Boundary Mixing. *Journal of Physical Oceanography*, **47** (2), 261–283, doi:10.1175/
994 JPO-D-16-0082.1, URL <https://journals.ametsoc.org/doi/full/10.1175/JPO-D-16-0082>.
995 1, publisher: American Meteorological Society.

996 Melet, A., R. Hallberg, S. Legg, and M. Nikurashin, 2014: Sensitivity of the Ocean
997 State to Lee Wave–Driven Mixing. *Journal of Physical Oceanography*, **44** (3), 900–
998 921, doi:10.1175/JPO-D-13-072.1, URL <http://journals.ametsoc.org/doi/abs/10.1175/>
999 [JPO-D-13-072.1](http://journals.ametsoc.org/doi/abs/10.1175/JPO-D-13-072.1).

1000 Morris, M. Y., M. M. Hall, L. C. S. Laurent, and N. G. Hogg, 2001: Abyssal Mixing in
1001 the Brazil Basin. *Journal of Physical Oceanography*, **31** (11), 3331–3348, doi:10.1175/
1002 1520-0485(2001)031<3331:AMITBB>2.0.CO;2, URL [https://journals.ametsoc.org/view/
1003 journals/phoc/31/11/1520-0485_2001_031_3331_amitbb_2.0.co_2.xml](https://journals.ametsoc.org/view/journals/phoc/31/11/1520-0485_2001_031_3331_amitbb_2.0.co_2.xml), publisher: Ameri-
1004 can Meteorological Society Section: Journal of Physical Oceanography.

1005 Munk, W. H., 1966: Abyssal recipes. *Deep Sea Research and Oceanographic Ab-*
1006 *stracts*, **13** (4), 707–730, doi:10.1016/0011-7471(66)90602-4, arXiv: cs/9605103 ISBN:
1007 1600117471.

1008 Naveira Garabato, A. C., and Coauthors, 2019: Rapid mixing and exchange of deep-ocean
1009 waters in an abyssal boundary current. *Proceedings of the National Academy of Sci-*
1010 *ences*, **116** (27), 13 233–13 238, doi:10.1073/pnas.1904087116, URL [https://www.pnas.](https://www.pnas.org/content/116/27/13233)
1011 [org/content/116/27/13233](https://www.pnas.org/content/116/27/13233), iSBN: 9781904087113 Publisher: National Academy of Sci-
1012 ences Section: Physical Sciences.

1013 Nazarian, R. H., C. M. Burns, S. Legg, M. C. Buijsman, H. Kaur, and
1014 B. K. Arbic, 2021: On the Magnitude of Canyon-Induced Mixing. *Jour-*
1015 *nal of Geophysical Research: Oceans*, **126** (11), e2021JC017 671, doi:10.1029/
1016 2021JC017671, URL <https://onlinelibrary.wiley.com/doi/abs/10.1029/2021JC017671>,
1017 _eprint: <https://onlinelibrary.wiley.com/doi/pdf/10.1029/2021JC017671>.

1018 Nikurashin, M., and R. Ferrari, 2013: Overturning circulation driven by breaking internal
1019 waves in the deep ocean. *Geophysical Research Letters*, **40** (12), 3133–3137, doi:10.1002/
1020 grl.50542, URL <http://doi.wiley.com/10.1002/grl.50542>, publisher: Wiley-Blackwell.

1021 Nikurashin, M., and S. Legg, 2011: A Mechanism for Local Dissipation of Internal Tides Gen-
1022 erated at Rough Topography. *Journal of Physical Oceanography*, **41** (2), 378–395, doi:10.
1023 1175/2010JPO4522.1, URL [http://journals.ametsoc.org/doi/abs/10.1175/2010JPO4522.](http://journals.ametsoc.org/doi/abs/10.1175/2010JPO4522.1)
1024 1.

1025 Peterson, H. G., and J. Callies, 2021: Rapid spin up and spin down of flow along slopes.
1026 *Journal of Physical Oceanography*, **-1** (aop), doi:10.1175/JPO-D-21-0173.1, URL [https://](https://journals.ametsoc.org/view/journals/phoc/aop/JPO-D-21-0173.1/JPO-D-21-0173.1.xml)
1027 journals.ametsoc.org/view/journals/phoc/aop/JPO-D-21-0173.1/JPO-D-21-0173.1.xml,
1028 publisher: American Meteorological Society Section: Journal of Physical Oceanography.

- 1029 Phillips, O., 1970: On flows induced by diffusion in a stably stratified fluid. *Deep Sea Re-*
1030 *search and Oceanographic Abstracts*, **17 (3)**, 435–443, doi:10.1016/0011-7471(70)90058-6,
1031 URL <http://linkinghub.elsevier.com/retrieve/pii/0011747170900586>.
- 1032 Plumb, R. A., and R. Ferrari, 2005: Transformed Eulerian-Mean Theory. Part I: Nonquasi-
1033 geostrophic Theory for Eddies on a Zonal-Mean Flow. *Journal of Physical Oceanography*,
1034 **35 (2)**, 165–174, doi:10.1175/JPO-2669.1, URL <http://journals.ametsoc.org/doi/abs/10.1175/JPO-2669.1>.
- 1036 Polzin, K., J. Toole, J. R. Ledwell, and R. Schmitt, 1997: Spatial Variability of Tur-
1037 bulent Mixing in the Spatial Variability Abyssal Ocean. *Science*, **276 (5309)**, 93–96,
1038 doi:10.1126/science.276.5309.93, URL [http://www.sciencemag.org/cgi/content/abstract/](http://www.sciencemag.org/cgi/content/abstract/276/5309/93)
1039 [276/5309/93](http://www.sciencemag.org/cgi/content/abstract/276/5309/93), iISBN: 0036-8075.
- 1040 Polzin, K. L., 2009: An abyssal recipe. *Ocean Modelling*, **30 (4)**, 298–309, doi:10.1016/j.
1041 [ocemod.2009.07.006](http://www.sciencedirect.com/science/article/pii/S0966759109000606).
- 1042 Polzin, K. L., and T. J. McDougall, 2022: Chapter 7 - Mixing at the ocean’s bottom bound-
1043 ary. *Ocean Mixing*, M. Meredith, and A. Naveira Garabato, Eds., Elsevier, 145–180,
1044 doi:10.1016/B978-0-12-821512-8.00014-1, URL [https://www.sciencedirect.com/science/](https://www.sciencedirect.com/science/article/pii/B9780128215128000141)
1045 [article/pii/B9780128215128000141](https://www.sciencedirect.com/science/article/pii/B9780128215128000141).
- 1046 Polzin, K. L., B. Wang, Z. Wang, F. Thwaites, and A. J. Williams, 2021: Moored Flux and
1047 Dissipation Estimates from the Northern Deepwater Gulf of Mexico. *Fluids*, **6 (7)**, 237,
1048 doi:10.3390/fluids6070237, URL <https://www.mdpi.com/2311-5521/6/7/237>, number: 7
1049 Publisher: Multidisciplinary Digital Publishing Institute.

- 1050 Pratt, L., and J. Whitehead, 2008: *Rotating Hydraulics: Nonlinear Topographic Effects in*
1051 *the Ocean and Atmosphere.*
- 1052 Rhines, P. B., and W. R. Young, 1982: Homogenization of potential vorticity in planetary
1053 gyres. *Journal of Fluid Mechanics*, **122** (-1), 347, doi:10.1017/S0022112082002250, URL
1054 http://www.journals.cambridge.org/abstract_S0022112082002250.
- 1055 Ruan, X., and J. Callies, 2020: Mixing-Driven Mean Flows and Submesoscale Eddies over
1056 Mid-Ocean Ridge Flanks and Fracture Zone Canyons. *Journal of Physical Oceanogra-*
1057 *phy*, **50** (1), 175–195, doi:10.1175/JPO-D-19-0174.1, URL [https://journals.ametsoc.org/](https://journals.ametsoc.org/view/journals/phoc/50/1/jpo-d-19-0174.1.xml)
1058 [view/journals/phoc/50/1/jpo-d-19-0174.1.xml](https://journals.ametsoc.org/view/journals/phoc/50/1/jpo-d-19-0174.1.xml), publisher: American Meteorological Soci-
1059 ety Section: Journal of Physical Oceanography.
- 1060 Salmun, H., P. D. Killworth, and J. R. Blundell, 1991: A two-dimensional model of boundary
1061 mixing. *Journal of Geophysical Research: Oceans*, **96** (C10), 18 447–18 474, doi:10.1029/
1062 [91JC01917](https://agupubs.onlinelibrary.wiley.com/doi/abs/10.1029/91JC01917), URL <https://agupubs.onlinelibrary.wiley.com/doi/abs/10.1029/91JC01917>.
- 1063 Smith, W. H. F., and D. T. Sandwell, 1997: Global Sea Floor Topography from Satel-
1064 lite Altimetry and Ship Depth Soundings. *Science*, **277** (5334), 1956–1962, doi:10.1126/
1065 [science.277.5334.1956](https://science.sciencemag.org/content/277/5334/1956), URL <https://science.sciencemag.org/content/277/5334/1956>, pub-
1066 lisher: American Association for the Advancement of Science Section: Research Article.
- 1067 Spingys, C. P., A. C. N. Garabato, S. Legg, K. L. Polzin, E. P. Abrahamson, C. E. Buck-
1068 ingham, A. Forryan, and E. E. Frajka-Williams, 2021: Mixing and Transformation in
1069 a Deep Western Boundary Current: A Case Study. *Journal of Physical Oceanography*,
1070 **51** (4), 1205–1222, doi:10.1175/JPO-D-20-0132.1, URL [https://journals.ametsoc.org/](https://journals.ametsoc.org/view/journals/phoc/aop/JPO-D-20-0132.1/JPO-D-20-0132.1.xml)
1071 [view/journals/phoc/aop/JPO-D-20-0132.1/JPO-D-20-0132.1.xml](https://journals.ametsoc.org/view/journals/phoc/aop/JPO-D-20-0132.1/JPO-D-20-0132.1.xml), publisher: American
1072 Meteorological Society Section: Journal of Physical Oceanography.

1073 St. Laurent, L., and C. Garrett, 2002: The Role of Internal Tides in Mixing the
1074 Deep Ocean. *Journal of Physical Oceanography*, **32** (10), 2882–2899, doi:10.1175/
1075 1520-0485(2002)032(2882:TROITI)2.0.CO;2, URL [http://journals.ametsoc.org/doi/abs/
1076 10.1175/1520-0485%282002%29032%3C2882%3ATROITI%3E2.0.CO%3B2](http://journals.ametsoc.org/doi/abs/10.1175/1520-0485%282002%29032%3C2882%3ATROITI%3E2.0.CO%3B2).

1077 St. Laurent, L. C., J. M. Toole, and R. W. Schmitt, 2001: Buoyancy Forcing by Turbulence
1078 above Rough Topography in the Abyssal Brazil Basin*. *Journal of Physical Oceanography*,
1079 **31** (12), 3476–3495, doi:10.1175/1520-0485(2001)031<3476:BFBTAR>2.0.CO;2.

1080 Stommel, H., 1958: The abyssal circulation. *Deep Sea Research (1953)*, **5** (1), 80–
1081 82, doi:10.1016/S0146-6291(58)80014-4, URL [https://www.sciencedirect.com/science/
1082 article/pii/S0146629158800144](https://www.sciencedirect.com/science/article/pii/S0146629158800144).

1083 Stone, P. H., 1966: On Non-Geostrophic Baroclinic Stability. *Journal of the Atmo-*
1084 *spheric Sciences*, **23** (4), 390–400, doi:10.1175/1520-0469(1966)023<0390:ONGBS>2.0.
1085 CO;2, URL [https://journals.ametsoc.org/view/journals/atsc/23/4/1520-0469_1966_023_
1086 0390_ongbs_2_0_co_2.xml](https://journals.ametsoc.org/view/journals/atsc/23/4/1520-0469_1966_023_0390_ongbs_2_0_co_2.xml), publisher: American Meteorological Society Section: Journal
1087 of the Atmospheric Sciences.

1088 Sverdrup, H., M. Johnson, and R. Fleming, 1942: The Oceans: Their Physics, Chemistry
1089 and General Biology. *Oceanography*, 1104, doi:10.2307/210609, arXiv: 1011.1669v3 ISBN:
1090 9788578110796.

1091 Talley, L. D., 2013: Closure of the Global Overturning Circulation Through the Indian,
1092 Pacific, and Southern Oceans: Schematics and Transports. *Oceanography*, **26** (1), 80–97,
1093 doi:10.5670/oceanog.2013.07, URL [http://apps.webofknowledge.com/full_record.do?
1094 product=UA&search_mode=GeneralSearch&qid=14&SID=W1jPgX8kkS6brME6NvD&
1095 page=1&doc=1](http://apps.webofknowledge.com/full_record.do?product=UA&search_mode=GeneralSearch&qid=14&SID=W1jPgX8kkS6brME6NvD&page=1&doc=1), arXiv: 1011.1669v3 ISBN: 1042-8275.

- 1096 Talley, L. D., J. L. Reid, and P. E. Robbins, 2003: Data-Based Meridional Overturning
1097 Streamfunctions for the Global Ocean. *Journal of Climate*, **16** (19), 3213–3226, doi:
1098 10.1175/1520-0442(2003)016<3213:DAMOSFT>2.0.CO;2, URL [https://journals.ametsoc.
1099 org/view/journals/clim/16/19/1520-0442_2003_016_3213_dmosft_2.0.co_2.xml](https://journals.ametsoc.org/view/journals/clim/16/19/1520-0442_2003_016_3213_dmosft_2.0.co_2.xml), publisher:
1100 American Meteorological Society Section: Journal of Climate.
- 1101 Taylor, G. I., and W. N. Shaw, 1920: I. Tidal friction in the Irish Sea. *Philosophical
1102 Transactions of the Royal Society of London. Series A, Containing Papers of a Math-
1103 ematical or Physical Character*, **220** (571-581), 1–33, doi:10.1098/rsta.1920.0001, URL
1104 <https://royalsocietypublishing.org/doi/10.1098/rsta.1920.0001>, publisher: Royal Society.
- 1105 Thompson, L., and G. C. Johnson, 1996: Abyssal currents generated by diffusion and
1106 geothermal heating over rises. *Deep Sea Research Part I: Oceanographic Research Pa-
1107 pers*, **43** (2), 193–211, doi:10.1016/0967-0637(96)00095-7, URL [http://www.sciencedirect.
1108 com/science/article/pii/0967063796000957](http://www.sciencedirect.com/science/article/pii/0967063796000957).
- 1109 Thorpe, S. A., 1987: Current and Temperature Variability on the Continental Slope.
1110 *Philosophical Transactions of the Royal Society A: Mathematical, Physical and Engi-
1111 neering Sciences*, **323** (1574), 471–517, doi:10.1098/rsta.1987.0100, URL [http://rsta.
1112 royalsocietypublishing.org/cgi/doi/10.1098/rsta.1987.0100](http://rsta.royalsocietypublishing.org/cgi/doi/10.1098/rsta.1987.0100), publisher: The Royal Society.
- 1113 Thorpe, S. A., 2005: *The Turbulent Ocean*. Cambridge University Press, Cam-
1114 bridge, doi:10.1017/CBO9780511819933, URL [https://www.cambridge.org/core/books/
1115 turbulent-ocean/1F9A34350F4AA077CA27641C6884B61B](https://www.cambridge.org/core/books/turbulent-ocean/1F9A34350F4AA077CA27641C6884B61B).
- 1116 Thurnherr, A. M., 2000: Hydrography and flow in the rift valley of the Mid-Atlantic Ridge.
1117 phd, University of Southampton, URL <https://eprints.soton.ac.uk/42174/>.

- 1118 Thurnherr, A. M., L. Clément, L. S. Laurent, R. Ferrari, and T. Ijichi, 2020: Transformation
1119 and Upwelling of Bottom Water in Fracture Zone Valleys. *Journal of Physical Oceanog-*
1120 *raphy*, **50** (3), 715–726, doi:10.1175/JPO-D-19-0021.1, URL [https://journals.ametsoc.](https://journals.ametsoc.org/view/journals/phoc/50/3/jpo-d-19-0021.1.xml)
1121 [org/view/journals/phoc/50/3/jpo-d-19-0021.1.xml](https://journals.ametsoc.org/view/journals/phoc/50/3/jpo-d-19-0021.1.xml), publisher: American Meteorological
1122 Society Section: Journal of Physical Oceanography.
- 1123 Thurnherr, A. M., and K. G. Speer, 2003: Boundary Mixing and Topographic
1124 Blocking on the Mid-Atlantic Ridge in the South Atlantic*. *Journal of Physi-*
1125 *cal Oceanography*, **33** (4), 848–862, doi:10.1175/1520-0485(2003)33<848:BMATBO>2.
1126 0.CO;2, URL [http://journals.ametsoc.org/doi/abs/10.1175/1520-0485%282003%2933%](http://journals.ametsoc.org/doi/abs/10.1175/1520-0485%282003%2933%3C848%3ABMATBO%3E2.0.CO%3B2)
1127 [3C848%3ABMATBO%3E2.0.CO%3B2](http://journals.ametsoc.org/doi/abs/10.1175/1520-0485%282003%2933%3C848%3ABMATBO%3E2.0.CO%3B2).
- 1128 Thurnherr, A. M., and Coauthors, 2005: Mixing Associated with Sills in a Canyon on
1129 the Midocean Ridge Flank*. *Journal of Physical Oceanography*, **35** (8), 1370–1381, doi:
1130 10.1175/JPO2773.1, URL <http://journals.ametsoc.org/doi/abs/10.1175/JPO2773.1>.
- 1131 Toole, J. M., 2007: Temporal Characteristics of Abyssal Finescale Motions above Rough
1132 Bathymetry. *Journal of Physical Oceanography*, **37** (3), 409–427, doi:10.1175/JPO2988.
1133 1, URL <https://journals.ametsoc.org/view/journals/phoc/37/3/jpo2988.1.xml>, publisher:
1134 American Meteorological Society Section: Journal of Physical Oceanography.
- 1135 Tozer, B., D. T. Sandwell, W. H. F. Smith, C. Olson, J. R. Beale, and P. Wes-
1136 sel, 2019: Global Bathymetry and Topography at 15 Arc Sec: SRTM15+.
1137 *Earth and Space Science*, **6** (10), 1847–1864, doi:10.1029/2019EA000658, URL
1138 <https://agupubs.onlinelibrary.wiley.com/doi/abs/10.1029/2019EA000658>, eprint:
1139 <https://agupubs.onlinelibrary.wiley.com/doi/pdf/10.1029/2019EA000658>.

- 1140 Tziperman, E., 1986: On the Role of Interior Mixing and Air-Sea Fluxes in De-
1141 termining the Stratification and Circulation of the Oceans. *Journal of Physical*
1142 *Oceanography*, **16** (4), 680–693, doi:10.1175/1520-0485(1986)016<0680:OTROIM>2.0.
1143 CO;2, URL [https://journals.ametsoc.org/view/journals/phoc/16/4/1520-0485_1986_016_](https://journals.ametsoc.org/view/journals/phoc/16/4/1520-0485_1986_016_0680_otroim_2_0_co_2.xml)
1144 [0680_otroim_2_0_co_2.xml](https://journals.ametsoc.org/view/journals/phoc/16/4/1520-0485_1986_016_0680_otroim_2_0_co_2.xml), publisher: American Meteorological Society Section: Journal
1145 of Physical Oceanography.
- 1146 van Haren, H., 2018: High-Resolution Observations of Internal Wave Turbulence in the
1147 Deep Ocean. *The Ocean in Motion: Circulation, Waves, Polar Oceanography*, M. G.
1148 Velarde, R. Y. Tarakanov, and A. V. Marchenko, Eds., Springer Oceanography, Springer
1149 International Publishing, Cham, 127–146, doi:10.1007/978-3-319-71934-4_11, URL https://doi.org/10.1007/978-3-319-71934-4_11.
1150
- 1151 Voet, G., J. B. Girton, M. H. Alford, G. S. Carter, J. M. Klymak, and J. B. Mickett,
1152 2015: Pathways, Volume Transport, and Mixing of Abyssal Water in the Samoan Pas-
1153 sassage. *Journal of Physical Oceanography*, **45** (2), 562–588, doi:10.1175/JPO-D-14-0096.1,
1154 URL <https://journals.ametsoc.org/view/journals/phoc/45/2/jpo-d-14-0096.1.xml>, pub-
1155 lisher: American Meteorological Society Section: Journal of Physical Oceanography.
- 1156 Walin, G., 1982: On the relation between sea-surface heat flow and thermal circulation in
1157 the ocean. *Tellus*, **34** (2), 187–195, doi:10.3402/tellusa.v34i2.10801, URL [https://doi.org/](https://doi.org/10.3402/tellusa.v34i2.10801)
1158 [10.3402/tellusa.v34i2.10801](https://doi.org/10.3402/tellusa.v34i2.10801).
- 1159 Watson, A. J., J. R. Ledwell, D. J. Webb, and C. Wunsch, 1988: Purposefully Released
1160 Tracers [and Discussion]. *Philosophical Transactions of the Royal Society of London. Series*
1161 *A, Mathematical and Physical Sciences*, **325** (1583), 189–200, URL [https://www.jstor.](https://www.jstor.org/stable/38109)
1162 [org/stable/38109](https://www.jstor.org/stable/38109), publisher: The Royal Society.

- 1163 Wenegrat, J. O., J. Callies, and L. N. Thomas, 2018: Submesoscale Baroclinic Insta-
1164 bility in the Bottom Boundary Layer. *Journal of Physical Oceanography*, JPO-D-17-
1165 0264.1, doi:10.1175/JPO-D-17-0264.1, URL [http://journals.ametsoc.org/doi/10.1175/
1166 JPO-D-17-0264.1](http://journals.ametsoc.org/doi/10.1175/JPO-D-17-0264.1).
- 1167 Whalen, C. B., 2021: Best Practices for Comparing Ocean Turbulence Measurements across
1168 Spatiotemporal Scales. *Journal of Atmospheric and Oceanic Technology*, **38** (4), 837-
1169 841, doi:10.1175/JTECH-D-20-0175.1, URL [https://journals.ametsoc.org/view/journals/
1170 atot/38/4/JTECH-D-20-0175.1.xml](https://journals.ametsoc.org/view/journals/atot/38/4/JTECH-D-20-0175.1.xml), publisher: American Meteorological Society Section:
1171 Journal of Atmospheric and Oceanic Technology.
- 1172 Whalen, C. B., C. de Lavergne, A. C. Naveira Garabato, J. M. Klymak, J. A. MacKinnon,
1173 and K. L. Sheen, 2020: Internal wave-driven mixing: governing processes and conse-
1174 quences for climate. *Nature Reviews Earth & Environment*, **1** (11), 606-621, doi:10.1038/
1175 s43017-020-0097-z, URL <https://www.nature.com/articles/s43017-020-0097-z>, number:
1176 11 Publisher: Nature Publishing Group.
- 1177 Winters, K. B., and L. Armi, 2012: Hydraulic control of continuously stratified flow over
1178 an obstacle. *Journal of Fluid Mechanics*, **700**, 502-513, doi:10.1017/jfm.2012.157,
1179 URL [https://www.cambridge.org/core/journals/journal-of-fluid-mechanics/
1180 article/abs/hydraulic-control-of-continuously-stratified-flow-over-an-obstacle/
1181 0A67346BF37CCA5EFACC92238FD92CA](https://www.cambridge.org/core/journals/journal-of-fluid-mechanics/article/abs/hydraulic-control-of-continuously-stratified-flow-over-an-obstacle/0A67346BF37CCA5EFACC92238FD92CA), publisher: Cambridge University Press.
- 1182 Wunsch, C., 1970: On oceanic boundary mixing. *Deep-Sea Research and Oceanographic*
1183 *Abstracts*, **17** (2), 293-301, doi:10.1016/0011-7471(70)90022-7.
- 1184 Young, W. R., 2011: An Exact Thickness-Weighted Average Formulation of the Boussi-
1185 nesq Equations. *Journal of Physical Oceanography*, **42** (5), 692-707, doi:10.1175/

1186 JPO-D-11-0102.1, URL <https://journals.ametsoc.org/doi/full/10.1175/JPO-D-11-0102>.

1187 1.

1188 LIST OF FIGURES

1189 **Fig. 1.** Height above bottom stratification profiles at steady state for 1D BBL models:
 1190 with the same external parameters as the BBTRE simulations (solid), without
 1191 rotation ($f = 0$; dotted), and with enhanced vertical diffusion of along-slope
 1192 momentum, $\sigma_v(z) \gg 1$ (dash-dotted; see Appendix). 61

1193 **Fig. 2.** A generalized slope-normal buoyancy budget (16), derived by integrating the
 1194 buoyancy equation below a given height above the mean slope z (volume shown
 1195 in light blue); at equilibrium, the mean up-slope transport (across the background
 1196 stratification N^2) into the box (blue lines) is given by the net flux of buoyancy
 1197 into the box from above (red line), $\Psi \propto -\langle -\kappa B_z \rangle - \langle wb \rangle$. We assume no buoyancy
 1198 flux across the seafloor (black line) at $z = \max(d) - d(x, y)$ 62

1199 **Fig. 3.** Numerical model domains. (a) Seafloor elevation $-\hat{d}(\hat{x}, \hat{y})$, including the doubly-
 1200 periodic simulation domain centered on the Brazil Basin Tracer Release Exper-
 1201 iment (BBTRE) canyon. Red markers show the locations of moorings from
 1202 Clément et al. (2017) (CTS17) and Thurnherr et al. (2005) (T05). The inset
 1203 highlights the DoMORE sill that dramatically constrains up-canyon flow. White
 1204 markers mark the injection location from the BBTRE (Ledwell et al. 2000). (b)
 1205 Imposed slope-normal diffusivity field, the result of applying a self-similar ex-
 1206 ponential profile as a function of the height-above-bottom (eq. 17) to variable
 1207 topography. Arrows show the original along-canyon \hat{y} and cross-canyon \hat{x} direc-
 1208 tions as well as the transformed slope-normal \mathbf{z} and along-canyon \mathbf{x} coordinate
 1209 vectors (a), which appear distorted because the vertical dimension is exagger-
 1210 ated (b). (c-f) A hierarchy of simulations with progressively complex seafloor
 1211 bathymetry geometries (relative to a constant mean slope of angle θ ; see dashed
 1212 lines in panel b). Thin black lines distinguish three sub-regions: the canyon
 1213 trough, the canyon’s flanks, and the ridge flank surrounding the canyon. 63

1214 **Fig. 4.** Structure of up-canyon mean flow in the BBTRE Canyon. (a) Along-canyon-
 1215 averaged up-canyon flow \bar{u}^x , with the mean canyon seafloor outlined in trans-
 1216 parent grey shading and cross-canyon thalweg shown in the dark gray shading.
 1217 (b) Cross-canyon-averaged up-canyon flow \bar{u}^y in the original coordinate frame
 1218 (\hat{x}, \hat{z}). Grey lines represent equally-spaced buoyancy surfaces. The much gentler
 1219 isopycnal slopes seen in some hydrographic sections of canyons, as in Thurnherr
 1220 et al. 2020, are largely an artifact of their much lower horizontal resolution, as
 1221 evidenced by the favorable comparison in Figure 6. The black line marks the
 1222 mean seafloor depth of the half of the domain furthest from the canyon thalweg
 1223 and acts as a proxy for the crest of the canyon. (c) Up-canyon flux, integrated
 1224 in the slope-normal direction z . Black and grey contours show a deep and shal-
 1225 low isobath, respectively, to highlight the canyon topography that shallows to
 1226 the right. (d) Same as (c), but integrated only from $z = 0$ m to $z = 800$ m to
 1227 highlight the core up-canyon jet within the canyon. 64

1228 **Fig. 5.** Structure of up-canyon flow at two mooring sites. (a,c) Cross-canyon sections
 1229 of the up-canyon flow at the locations of the DoMORE sill mooring (Clément
 1230 et al. 2017) (CTS17-P1) and the BBTRE mooring Thurnherr et al. (2005) (T05).
 1231 Light grey shading shows the local seafloor depth while the dark grey shading in
 1232 (a) shows the mean height of the canyon floor above the mean slope, highlighting
 1233 the significant vertical and cross-canyon constriction introduced by the sill. (b,d)
 1234 Height-above-bottom profiles of the up-canyon flow at the locations of the two
 1235 moorings (light grey lines) and shifted a few grid columns over to improve capture

1236 the core of the jet (black lines), which is somewhat displaced due to the coarse
 1237 model bathymetry. 65

1238 **Fig. 6.** Comparison between observed and simulated stratification in the BBTRE Canyon
 1239 region. (a) Height above bottom-averaged profile of stratification for the full
 1240 simulation domain (solid blue), for the sample-mean of nine co-located CTD casts
 1241 (dotted red; Ledwell et al. 2000), free-falling HRP-microstructure profiles (dashed
 1242 red; Polzin et al. 1997), and simulated CTD casts (solid red). The dashed blue
 1243 line shows the sample-mean of 10 HRP profiles that follow the canyon crest just
 1244 north of the domain. (b) Observed (solid) and simulated (dashed) density profiles
 1245 at the nine locations sampled by the BBTRE observational campaign, overlaid
 1246 on a map of the seafloor-elevation. An additional simulated profile typical of the
 1247 crest region outside of the canyon is also shown, revealing an apparent sampling
 1248 bias due to the strategy of measuring weakly-stratified deep depressions along
 1249 the trough of the canyon in search of the released tracer (Ledwell et al. 2000). 66

1250 **Fig. 7.** Instantaneous normalized relative vorticity ζ/f , or local Rossby number, in and
 1251 above the BBTRE Canyon at four different heights above the mean slope, at
 1252 $t = 5050$ days. 67

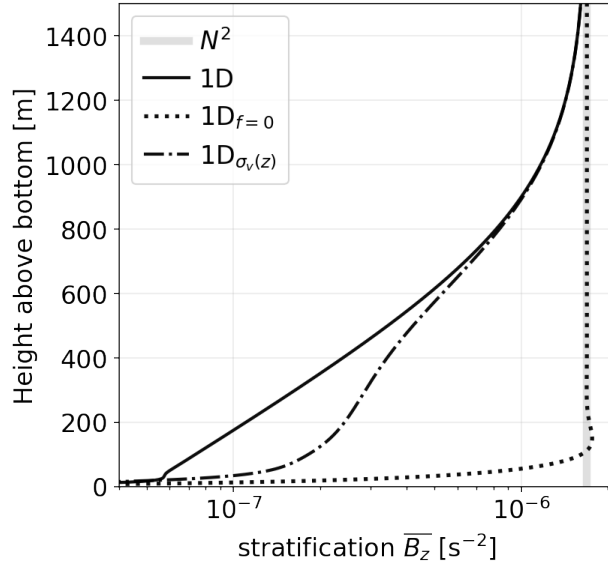
1253 **Fig. 8.** Generalized integral buoyancy budget in a hierarchy of increasingly complex simu-
 1254 lations of mixing-driven flows up a mean slope of angle θ : (a) 1D, (b) Smooth3D,
 1255 (c) $1D_{\sigma_v(z)}$, (d) Canyon, (e) Canyon+Sill, (f) BBTRE. Solid lines show terms
 1256 of the volume-integrated buoyancy budget (eq. 16), averaged over days 5000 to
 1257 5200, for a layer bounded by a given Height Above the Mean Slope (HAMS).
 1258 We interpret the sum of the Mean Flow and Eddy terms as a Residual Flow.
 1259 The left-hand-side tendencies (LHS) are equal to the remainder of the approx-
 1260 imate balance (RHS) between slope-normal turbulent diffusion and the cross-
 1261 slope residual circulation, which includes both mean and eddy components. We
 1262 divide (eq. 16) by the factor $N^2 L_x \sin \theta$ to conveniently express the budget
 1263 in terms of the quantity of interest, the up-slope volume transport Ψ with units of
 1264 $mSv \equiv 10^3 m^3/s$. Dotted lines in (a,c) show 1D steady state solutions and the
 1265 dashed red line shows the integral constraint (eq. 13); in panels a and b, some of
 1266 the dotted lines appear missing because they overlap with others. Grey shading
 1267 shows the HAMS range spanned by the canyon, if present. 68

1268 **Fig. 9.** Height above bottom-averaged stratification profiles at $t = 5000$ days, as a func-
 1269 tion of model complexity (lines) and domain sub-region (panels b & c). Panel
 1270 (a) and grey lines in (b,c) show one-dimensional solutions: with the same param-
 1271 eters as the BBTRE simulations (solid); without a mean-slope ($\theta = 0$; dashed),
 1272 without rotation ($f = 0$; dotted); and with an enhanced along-slope turbulent
 1273 Prandtl number $\sigma_v(z)$, a crude proxy for restratification by submesoscale baro-
 1274 clinic eddies (dash-dotted). Colored lines show a hierarchy of three-dimensional
 1275 simulations with increasingly complex topographies (see Figure 3c-f). Arrows
 1276 show how the stratification profiles evolve when processes are added: 1. adding
 1277 a mean-slope, 2. allowing three-dimensional eddies, 3. introducing a cross-slope
 1278 canyon, 4. blocking the canyon with a sill, and 5. adding realistic hills (i.e., the
 1279 BBTRE topography). 69

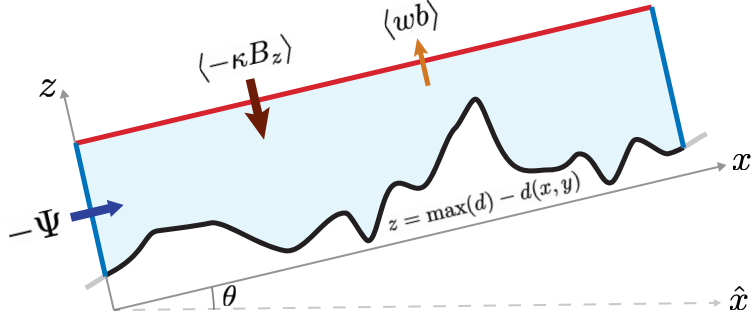
1280 **Fig. 10.** Cross-slope (left) and along-slope (right) sections of the stratification along the
 1281 trough of a canyon in a hierarchy of numerical simulations (Smooth3D has no
 1282 canyon, so the section is arbitrary). Solid grey lines in the left column show
 1283 the approximate elevation of the ridge flanks surrounding the canyon while in

1284 the right column they show HAMS of the topographic sill (if present). Dashed
 1285 grey lines show the locations of the respective sections. Black lines in panel (d)
 1286 represent equally-spaced buoyancy surfaces. 70

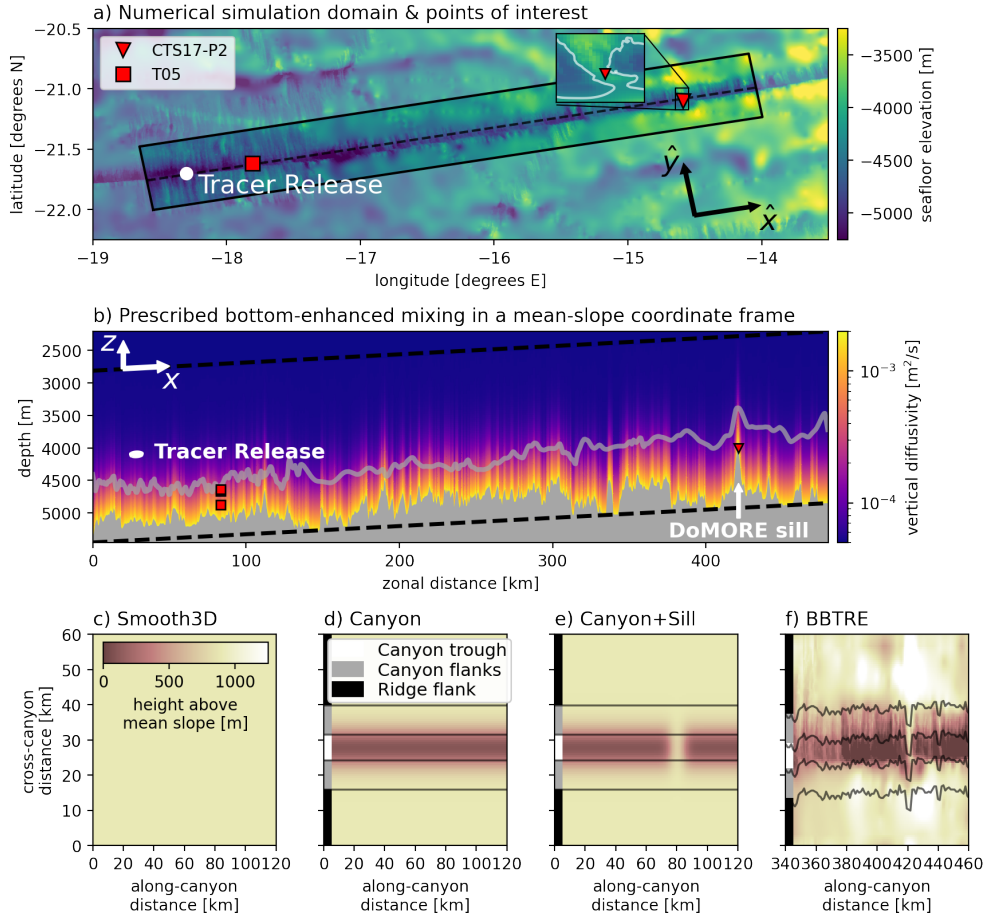
1287 **Fig. 11.**a) An idealized $\sigma_v(z)$ profile (dash-dotted) with vertical scale $\eta = 225$ m, tuned
 1288 to the Smooth3D model that resolves submesoscale baroclinic instabilities using
 1289 equation (A11; solid blue). b) The ratio of the mean isopycnal slope
 1290 $s_b = -N^2 \sin \theta / (N^2 \cos \theta + \bar{b}_z)$ to the horizontally-averaged eddy flux slope
 1291 $s = \frac{w'b'}{u'b'}$, which is $\mathcal{O}(1)$ outside of the strongly diabatic and frictional bottom
 1292 layer. The discontinuity near 750 m is due sign reversals in both the perturba-
 1293 tion stratification and the slope-normal eddy buoyancy flux, which enter in the
 1294 denominators of expressions for σ_v and s^{-1} , respectively. 71



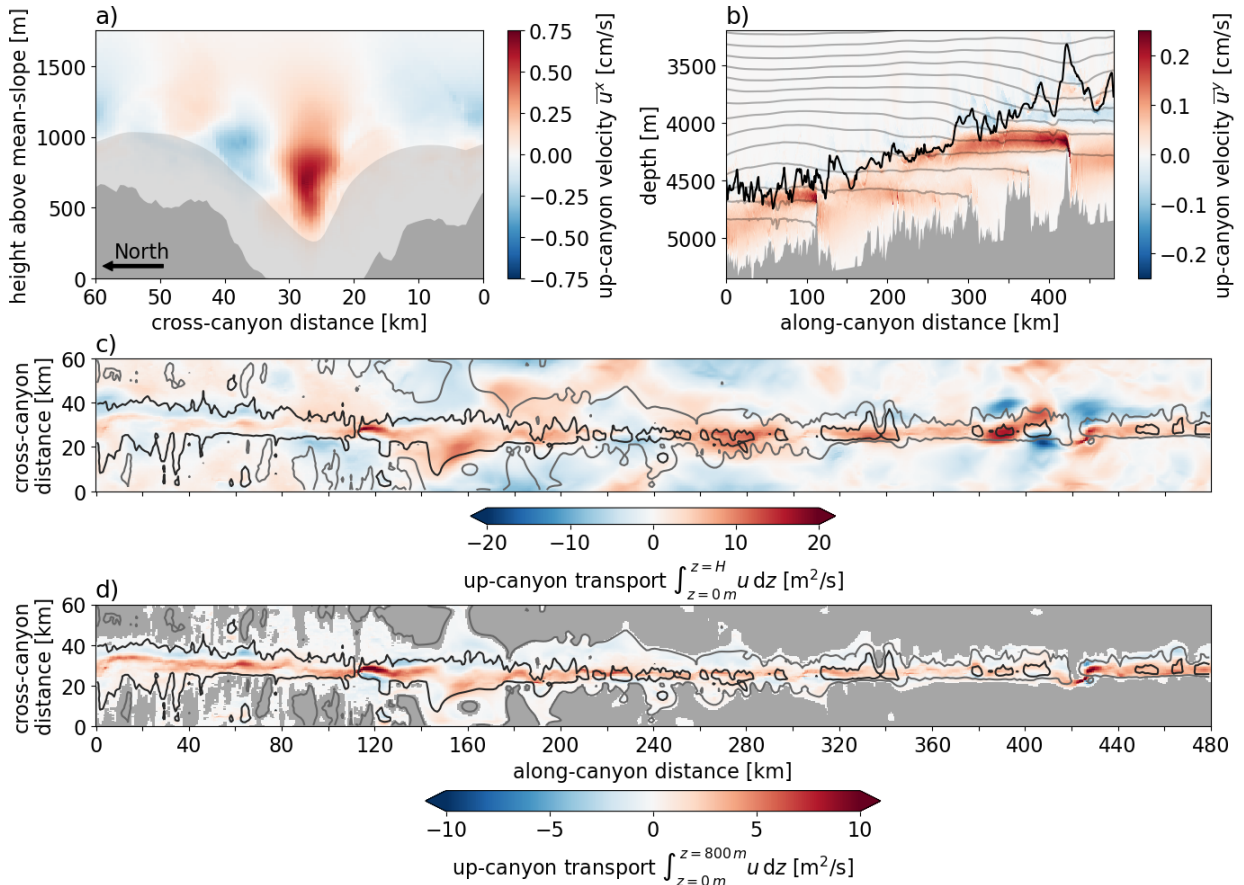
1295 FIG. 1. Height above bottom stratification profiles at steady state for 1D BBL models: with the
 1296 same external parameters as the BBTRE simulations (solid), without rotation ($f = 0$; dotted), and
 1297 with enhanced vertical diffusion of along-slope momentum, $\sigma_v(z) \gg 1$ (dash-dotted; see Appendix).



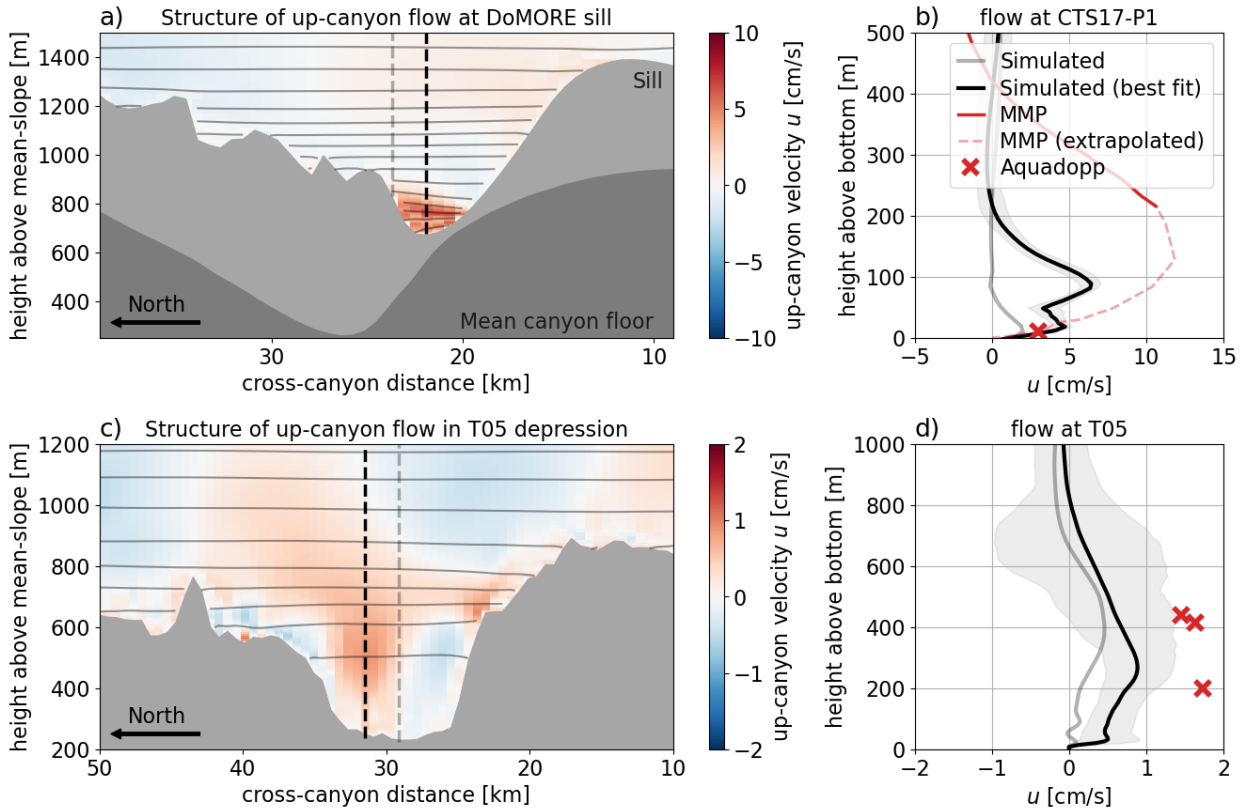
1298 FIG. 2. A generalized slope-normal buoyancy budget (16), derived by integrating the buoyancy
 1299 equation below a given height above the mean slope z (volume shown in light blue); at equilibrium,
 1300 the mean up-slope transport (across the background stratification N^2) into the box (blue lines) is
 1301 given by the net flux of buoyancy into the box from above (red line), $\Psi \propto -\langle -\kappa B_z \rangle - \langle wb \rangle$. We
 1302 assume no buoyancy flux across the seafloor (black line) at $z = \max(d) - d(x, y)$.



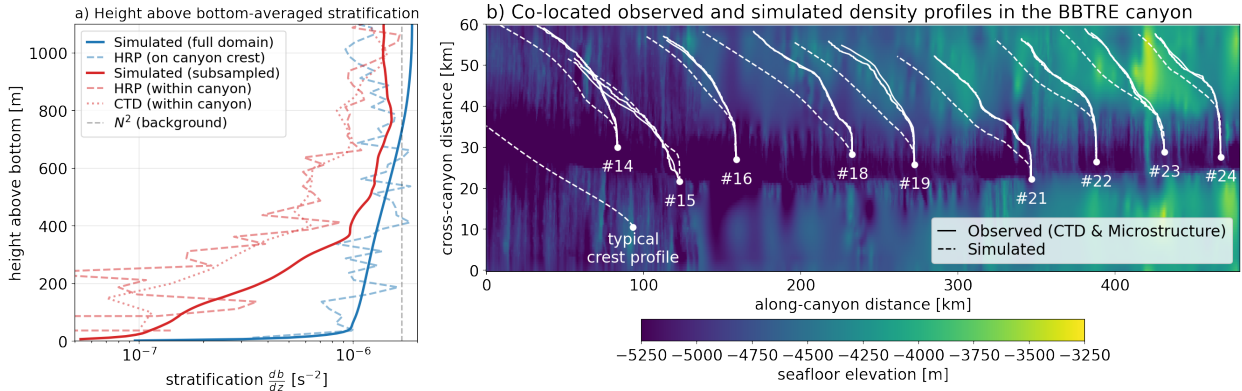
1303 FIG. 3. Numerical model domains. (a) Seafloor elevation $-\hat{d}(\hat{x}, \hat{y})$, including the doubly-periodic
 1304 simulation domain centered on the Brazil Basin Tracer Release Experiment (BBTRE) canyon. Red
 1305 markers show the locations of moorings from Clément et al. (2017) (CTS17) and Thurnherr et al.
 1306 (2005) (T05). The inset highlights the DoMORE sill that dramatically constrains up-canyon flow.
 1307 White markers mark the injection location from the BBTRE (Ledwell et al. 2000). (b) Imposed
 1308 slope-normal diffusivity field, the result of applying a self-similar exponential profile as a function of
 1309 the height-above-bottom (eq. 17) to variable topography. Arrows show the original along-canyon
 1310 \hat{y} and cross-canyon \hat{x} directions as well as the transformed slope-normal \mathbf{z} and along-canyon \mathbf{x}
 1311 coordinate vectors (a), which appear distorted because the vertical dimension is exaggerated (b).
 1312 (c-f) A hierarchy of simulations with progressively complex seafloor bathymetry geometries (relative
 1313 to a constant mean slope of angle θ ; see dashed lines in panel b). Thin black lines distinguish three
 1314 sub-regions: the canyon trough, the canyon's flanks, and the ridge flank surrounding the canyon.



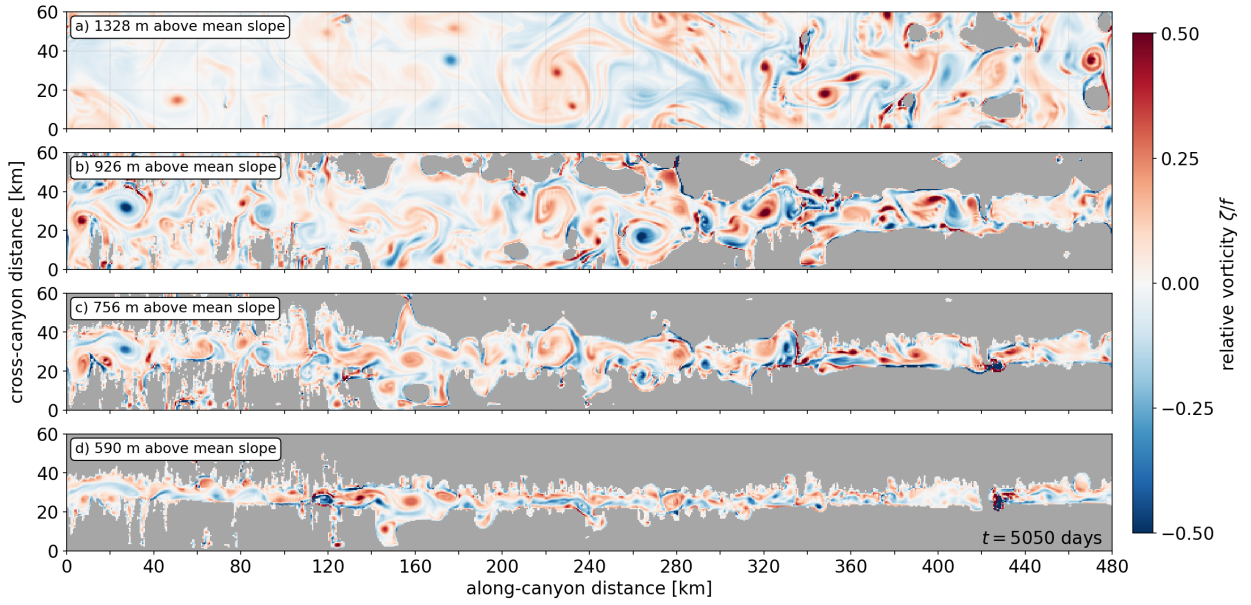
1315 FIG. 4. Structure of up-canyon mean flow in the BBTRE Canyon. (a) Along-canyon-averaged
 1316 up-canyon flow \bar{u}^x , with the mean canyon seafloor outlined in transparent grey shading and cross-
 1317 canyon thalweg shown in the dark gray shading. (b) Cross-canyon-averaged up-canyon flow \bar{u}^y
 1318 in the original coordinate frame (\hat{x}, \hat{z}) . Grey lines represent equally-spaced buoyancy surfaces. The
 1319 much gentler isopycnal slopes seen in some hydrographic sections of canyons, as in Thurnherr et al.
 1320 2020, are largely an artifact of their much lower horizontal resolution, as evidenced by the favorable
 1321 comparison in Figure 6. The black line marks the mean seafloor depth of the half of the domain
 1322 furthest from the canyon thalweg and acts as a proxy for the crest of the canyon. (c) Up-canyon
 1323 flux, integrated in the slope-normal direction z . Black and grey contours show a deep and shallow
 1324 isobath, respectively, to highlight the canyon topography that shallows to the right. (d) Same as
 1325 (c), but integrated only from $z = 0$ m to $z = 800$ m to highlight the core up-canyon jet within the
 1326 canyon.



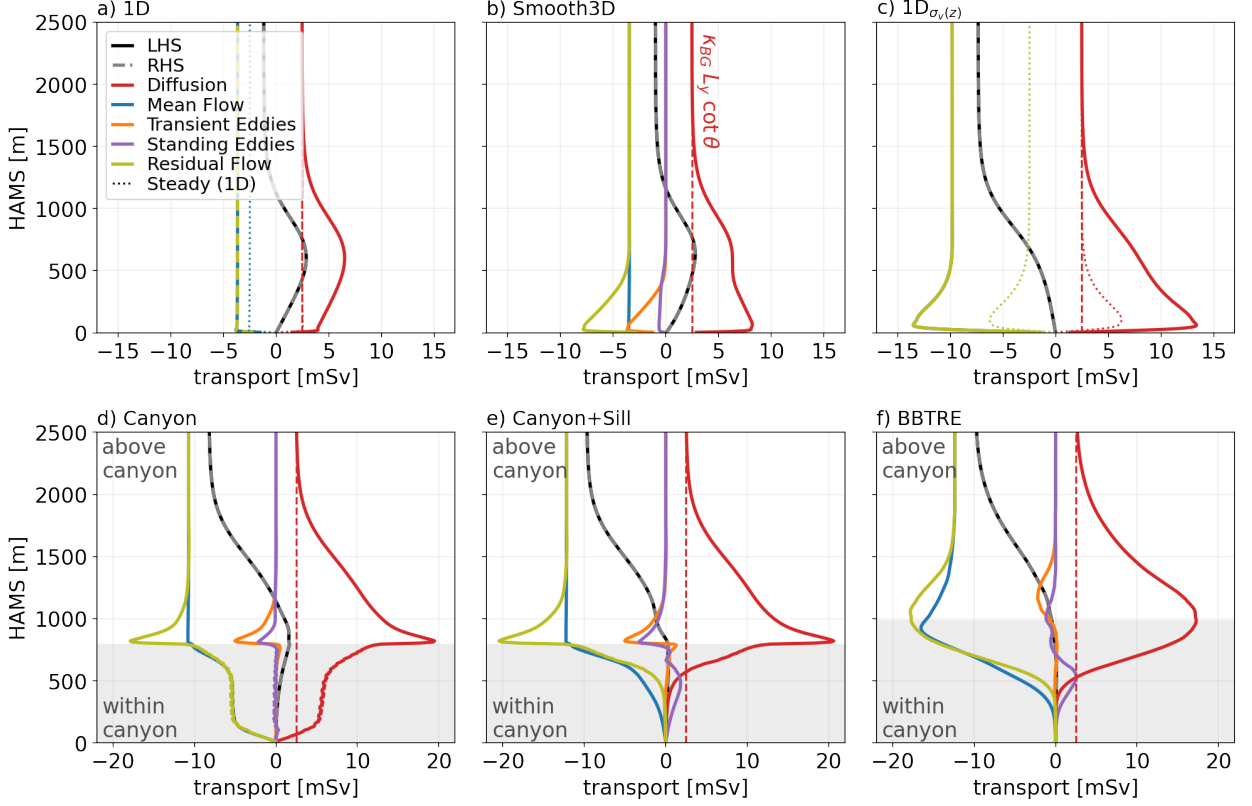
1327 FIG. 5. Structure of up-canyon flow at two mooring sites. (a,c) Cross-canyon sections of the up-
 1328 canyon flow at the locations of the DoMORE sill mooring (Clément et al. 2017) (CTS17-P1) and
 1329 the BBTRE mooring Thurnherr et al. (2005) (T05). Light grey shading shows the local seafloor
 1330 depth while the dark grey shading in (a) shows the mean height of the canyon floor above the
 1331 mean slope, highlighting the significant vertical and cross-canyon constriction introduced by the
 1332 sill. (b,d) Height-above-bottom profiles of the up-canyon flow at the locations of the two moorings
 1333 (light grey lines) and shifted a few grid columns over to improve capture the core of the jet (black
 1334 lines), which is somewhat displaced due to the coarse model bathymetry.



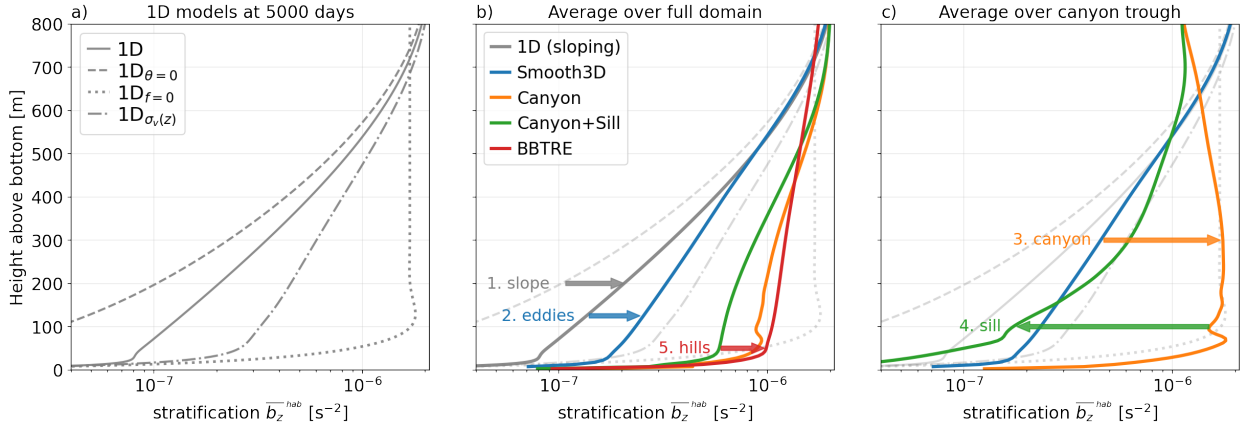
1335 FIG. 6. Comparison between observed and simulated stratification in the BBTRE Canyon region.
 1336 (a) Height above bottom-averaged profile of stratification for the full simulation domain (solid blue),
 1337 for the sample-mean of nine co-located CTD casts (dotted red; Ledwell et al. 2000), free-falling
 1338 HRP-microstructure profiles (dashed red; Polzin et al. 1997), and simulated CTD casts (solid red).
 1339 The dashed blue line shows the sample-mean of 10 HRP profiles that follow the canyon crest
 1340 just north of the domain. (b) Observed (solid) and simulated (dashed) density profiles at the
 1341 nine locations sampled by the BBTRE observational campaign, overlaid on a map of the seafloor-
 1342 elevation. An additional simulated profile typical of the crest region outside of the canyon is also
 1343 shown, revealing an apparent sampling bias due to the strategy of measuring weakly-stratified deep
 1344 depressions along the trough of the canyon in search of the released tracer (Ledwell et al. 2000).



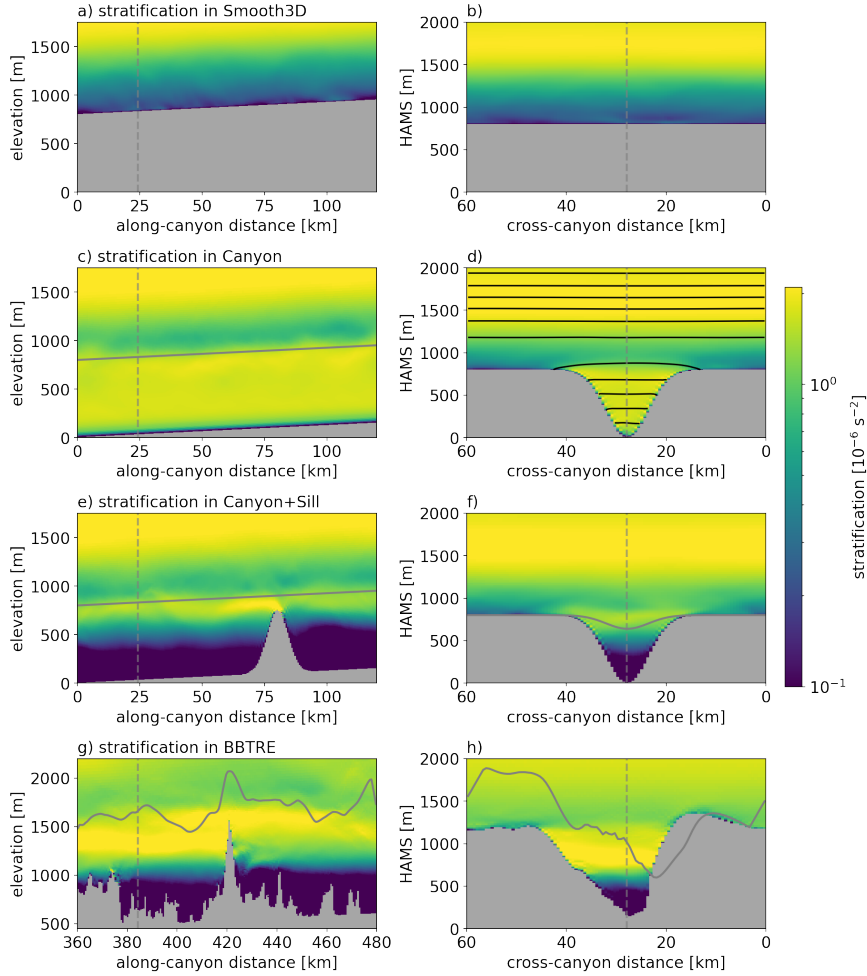
1345 FIG. 7. Instantaneous normalized relative vorticity ζ/f , or local Rossby number, in and above
 1346 the BBTRE Canyon at four different heights above the mean slope, at $t = 5050$ days.



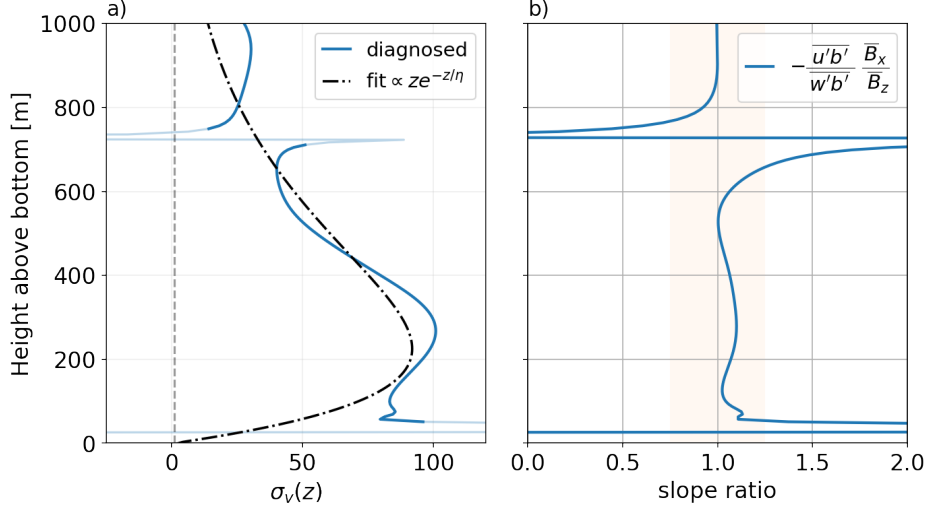
1347 FIG. 8. Generalized integral buoyancy budget in a hierarchy of increasingly complex simulations
 1348 of mixing-driven flows up a mean slope of angle θ : (a) 1D, (b) Smooth3D, (c) $1D_{\sigma_v(z)}$, (d) Canyon,
 1349 (e) Canyon+Sill, (f) BBTRE. Solid lines show terms of the volume-integrated buoyancy budget
 1350 (eq. 16), averaged over days 5000 to 5200, for a layer bounded by a given Height Above the Mean
 1351 Slope (HAMS). We interpret the sum of the Mean Flow and Eddy terms as a Residual Flow.
 1352 The left-hand-side tendencies (LHS) are equal to the remainder of the approximate balance (RHS)
 1353 between slope-normal turbulent diffusion and the cross-slope residual circulation, which includes
 1354 both mean and eddy components. We divide (eq. 16) by the factor $N^2 L_x \sin \theta$ to conveniently
 1355 express the budget in terms of the quantity of interest, the up-slope volume transport Ψ with units
 1356 of $\text{mSv} \equiv 10^3 \text{ m}^3/\text{s}$. Dotted lines in (a,c) show 1D steady state solutions and the dashed red line
 1357 shows the integral constraint (eq. 13); in panels a and b, some of the dotted lines appear missing
 1358 because they overlap with others. Grey shading shows the HAMS range spanned by the canyon, if
 1359 present.



1360 FIG. 9. Height above bottom-averaged stratification profiles at $t = 5000$ days, as a function of
 1361 model complexity (lines) and domain sub-region (panels b & c). Panel (a) and grey lines in (b,c)
 1362 show one-dimensional solutions: with the same parameters as the BBTRE simulations (solid);
 1363 without a mean-slope ($\theta = 0$; dashed), without rotation ($f = 0$; dotted); and with an enhanced
 1364 along-slope turbulent Prandtl number $\sigma_v(z)$, a crude proxy for restratification by submesoscale
 1365 baroclinic eddies (dash-dotted). Colored lines show a hierarchy of three-dimensional simulations
 1366 with increasingly complex topographies (see Figure 3c-f). Arrows show how the stratification
 1367 profiles evolve when processes are added: 1. adding a mean-slope, 2. allowing three-dimensional
 1368 eddies, 3. introducing a cross-slope canyon, 4. blocking the canyon with a sill, and 5. adding
 1369 realistic hills (i.e., the BBTRE topography).



1370 FIG. 10. Cross-slope (left) and along-slope (right) sections of the stratification along the trough
 1371 of a canyon in a hierarchy of numerical simulations (Smooth3D has no canyon, so the section is
 1372 arbitrary). Solid grey lines in the left column show the approximate elevation of the ridge flanks
 1373 surrounding the canyon while in the right column they show HAMS of the topographic sill (if
 1374 present). Dashed grey lines show the locations of the respective sections. Black lines in panel (d)
 1375 represent equally-spaced buoyancy surfaces.



1376 FIG. 11. a) An idealized $\sigma_v(z)$ profile (dash-dotted) with vertical scale $\eta = 225$ m, tuned to
 1377 the Smooth3D model that resolves submesoscale baroclinic instabilities using equation (A11; solid
 1378 blue). b) The ratio of the mean isopycnal slope $s_b = -N^2 \sin \theta / (N^2 \cos \theta + \bar{b}_z)$ to the horizontally-
 1379 averaged eddy flux slope $s = \frac{\overline{w'b'}}{\overline{u'b'}}$, which is $\mathcal{O}(1)$ outside of the strongly diabatic and frictional
 1380 bottom layer. The discontinuity near 750 m is due sign reversals in both the perturbation stratifi-
 1381 cation and the slope-normal eddy buoyancy flux, which enter in the denominators of expressions
 1382 for σ_v and s^{-1} , respectively.